Politecnico di Torino

Master of Science in Mechatronic Engineering
AY 2022/2023

Graduation Session: April 2023

Energy Recovery Assessment on Electric Bicycle Powertrain

Supervisors:

Prof. TONOLI Andrea

Prof. GALLUZZI Renato

Prof. ZENERINO Enrico Cesare

Candidate:

GENTILE Pietro

Abstract

The scientific community has widely recognized that pollution has reached a critical level and urgent action is needed to address this phenomenon. Exhaust emissions from conventionally fueled transportation systems are one of the major contributors to air pollution. To mitigate this problem, European Parliament decided to ban the sale of such vehicles by the year 2035. One potential solution to reduce pollution is the use of electric vehicles, including electric micro-mobility such as e-bikes, which have become increasingly popular in large cities due to their ability to reduce air pollution, traffic congestion, and parking problems, as well as offering a more sustainable mode of transportation. However, e-bikes still face limitations in terms of battery size, cost, and range.

Following an initial examination of the e-bikes market and possible configurations, this thesis aims to investigate the potential and limitations of an e-bike equipped with a parallel powertrain and a rear hub-mounted Permanent Magnet Synchronous Motor (PMSM). Emphasis is placed on optimizing the control of the PMSM incorporating regenerative braking: using the same PMSM as a generator, the vehicle is braked and energy, that would otherwise be dissipated during mechanical braking, is recovered. This regenerative braking technique can increase the battery life on a single run. A model of the electromechanical system is developed, and simulations are performed using driving cycles obtained from experimental tests. The simulation results are then validated with experimental data.

Finally, the thesis explores possibilities for future developments, particularly the development of energy management system. Studies about the efficiency of the human body during cycling are analyzed to develop algorithms for the management of the power flow, accounting not only for the optimal operating points of the electromechanical apparatus but also on the optimal operating points of the cyclist. Hence the goal is to optimize the overall efficiency of the system.

Index

List of Figures

List of Tables

CHAPTER 1 – Introduction

1.1 – Context of Thesis Work

In recent years, the issue of pollution and climate change has become a pressing concern, with widespread recognition of the criticality of this problem and the need for immediate solutions to address it. Among the most significant contributors to pollution and its harmful effects on the environment and human health is the road transport sector, which is the main responsible for the emission of a high volume of nitrogen oxides into the atmosphere [1]. This sector is particularly problematic in large urban areas, where air quality is at an all-time low, posing serious health risks to the local population. One of the most urgent challenges in this context is to find alternative modes of transport that can reduce pollution and mitigate the impact of conventionally powered transport systems.

Electric vehicles are emerging as a potential solution to this problem, and among them, e-bikes are gaining popularity due to their ability to reduce air pollution in cities and provide a safe and healthy alternative to classic vehicles. E-bikes offer a more sustainable mode of transport that is effective in reducing traffic congestion, which in turn reduces exhaust emissions into the air. They are particularly suitable for short to medium-distance trips in urban areas, where conventional vehicles are not only polluting but also contribute significantly to traffic congestion.

However, the definition of e-bikes is not universally consistent, and their features, including size, cost, and battery life, still pose significant challenges for widespread adoption. These limitations suggest that further research is needed in this area to develop increasingly efficient and safe e-bike systems that can deliver a range of benefits.

1.2 – Aim of the Thesis

The purpose of this thesis is to investigate the potential and limitations of an electric powertrain in an e-bike, with the electric motor located in the rear wheel hub. The electric motor belongs to the Permanent Magnet Synchronous Machines category and is designed specifically for this project by a team from the Politecnico di Torino [2]. The study focuses on analyzing the potential of Regenerative Braking and quantifying the amount of energy that can be recovered in various driving scenarios. Additionally, the study evaluates the additional range that this energy recovery corresponds to.

To achieve these objectives, a model of the electric powertrain is constructed, and an overall model representing the entire vehicle and rider is built around it. Simulations are conducted using experimentally acquired driving profiles, and the behavior of the electric powertrain, as well as the energy balance with Regenerative Braking, is evaluated. This analysis aims to provide a detailed understanding of the performance and energy efficiency of the electric powertrain and its potential for use in e-bikes. By quantifying the energy savings achieved through regenerative braking, the study aims to provide insights into the potential of e-bikes as a more sustainable and eco-friendly mode of transportation.

1.3 – Thesis Organization

The document comprises seven chapters, beginning with a brief introduction to the scope and objectives of the work. The second chapter presents a comprehensive overview of the state-of-the-art in e-bikes, analyzing the potential advantages of using these vehicles in urban environments and defining the different types of electric bicycles.

Chapter three details the mechanical and electrical system configuration required to construct the simulation model, while chapter four explores the mathematical model for synchronous electrical machines and examines the control techniques. The electric powertrain model is then developed in Simulink environment.

Chapter five outlines the overall vehicle model built around the electric powertrain model. It details the longitudinal dynamics of the e-bike and presents the control logic used to manage the power split between the cyclist and electric powertrain.

In chapter six, the developed model is used to conduct simulations and test the e-bike under various driving conditions, with the data collected and analyzed to verify the electric powertrain's correct functioning. In particular, the chapter examines the benefits of regenerative braking in different routes.

The final chapter, chapter seven, briefly outlines possible future developments for this project based on the research conducted, supported by relevant literature.

By providing a detailed analysis of the potential and limitations of e-bikes, this study could contribute to the development of more energy-efficient and environmentally friendly modes of transportation.

CHAPTER 2 – State of the Art

2.1 – Electric micro-mobility: a way to mitigate air pollution

The problem of environmental pollution has reached a critical level and has been a topic of public discussion for many years. Air pollution in large cities is globally recognized as a significant risk to the health of citizens [3]. The air pollution in urban scenario is mainly caused by the high density of conventional fuel vehicles emitting pollutants such as hydrocarbons, nitrogen oxides, carbon monoxide, and fine particulate matter [4]. The resulting poor air quality, congested roads, and poor traffic flow pose serious threats to public health and the quality of life and require personal and governmental actions to counter the issue.

A specific example can be seen in the metropolitan city of Turin in Italy, where geographic conformation, an important industrial apparatus, and high urban traffic density generate air quality below legislative limits, making it the most polluted city in Italy in 2022, with 98 days of exceeding the PM10 regulatory limits (35 days/year with an average above 50 micrograms/cubic meter) [5].

These are some of the reasons why the European Union has therefore decided to ban the sale of internal combustion vehicles (diesel and gasoline) by 2035 and transform the transport sector to carbon-neutral by 2040 [6], while promoting electric mobility as a strategy to reduce air pollution [7].

Electric mobility, that is the use of electric vehicles (EVs) for transportation, is becoming increasingly popular in modern cities as a way to reduce air pollution and greenhouse gas emissions, improve public health, and decrease dependence on fossil fuels. This is because electric vehicles produce zero tailpipe emissions and can be powered by a variety of sources, including renewable energy, reducing dependence on fossil fuels.

Electric mobility also has the advantage of being quieter than traditional internal combustion engine vehicles, reducing noise pollution in cities and making the urban environment more pleasant. The use of electric micro-mobility, such as lightweight devices or mini-vehicles, is gaining popularity as a flexible, sustainable, affordable, and on-demand transportation alternative for short-distance travel. In [8] is defined as innovative urban transportation solution aimed at providing short-distance travel options, including first and last-mile trips. Micro-mobility solutions include a range of lightweight devices or mini-vehicles that operate at a speed typically no greater than 45 km/h.

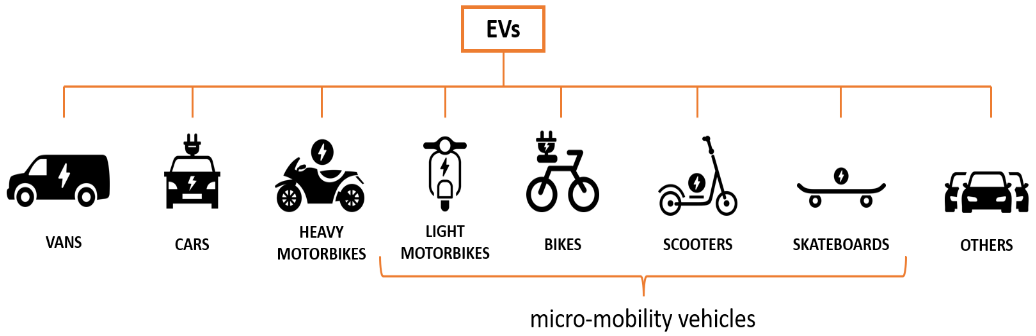

Figure 1 – Examples of e-vehicles

In particular, the use of two-wheeled electric vehicles as a means of transportation in cities has become increasingly popular in recent years. These vehicles have a tank-to-wheel energy consumption ranging from $1.5 \pm 0.5\, kW * h * 100km^{-1}$ for e-bikes to $7.0 \pm 3\, kW * h * 100km^{-1}$ for e-motorcycles, which is significantly more efficient than conventional two-wheelers like scooters ($25 \pm 9\, kW * h * 100km^{-1}$) and motorcycles ($41 \pm 13\, kW * h * 100km^{-1}$). However, using tank-to-wheel energy consumption alone to evaluate energy and environmental impact is insufficient. Thus, it is essential to consider other metrics that assess the overall environmental impact of the vehicle over its entire life cycle [9].

While this issue is critical for governments to make ecologically sustainable decisions, it is not the focus of this paper and will be not addressed.

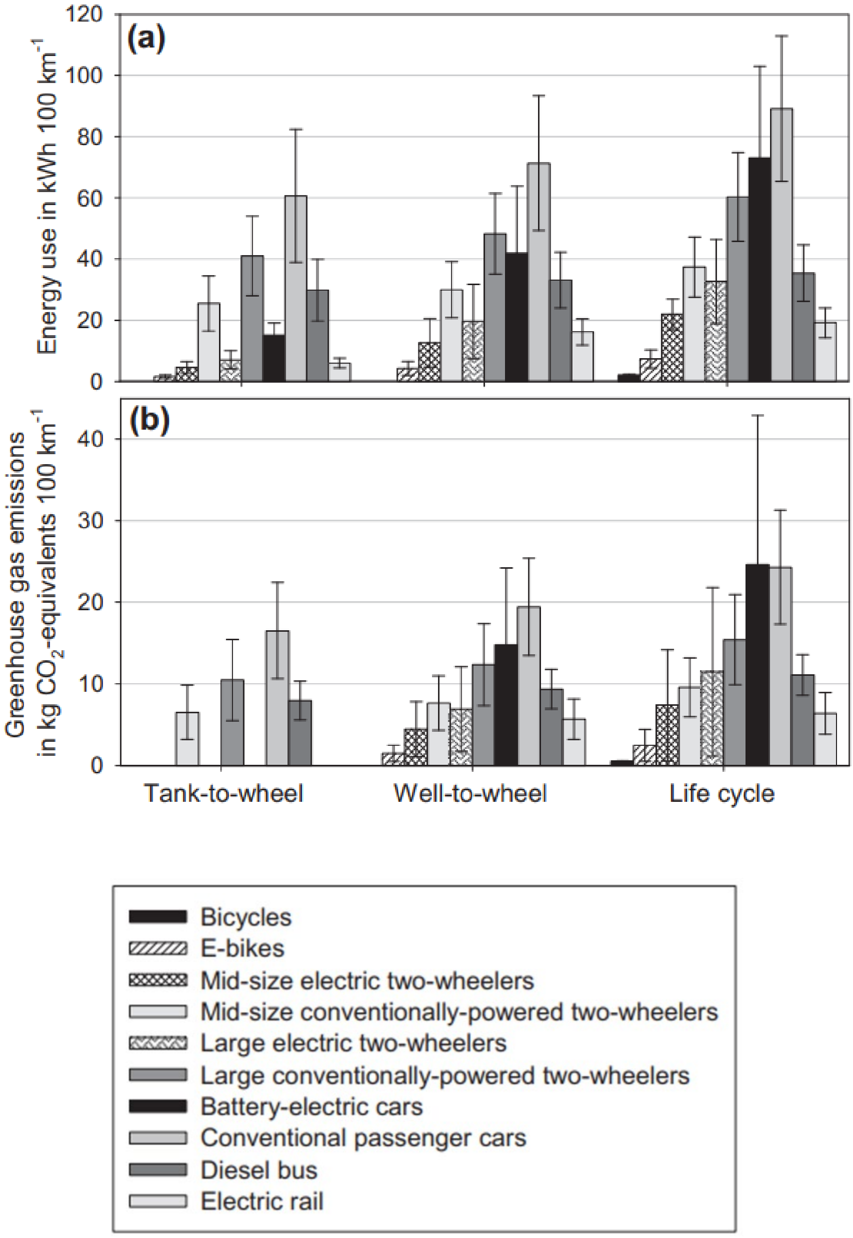
(a)
Energy use in kWh 100 km-1
120
100
80
60
40
20
0
(b)
Greenhouse gas emissions in kg CO2-equivalents 100 km-1
40
30
20
10
0
Tank-to-wheel
Well-to-wheel
Life cycle
Bicycles
E-bikes
Mid-size electric two-wheelers
Mid-size conventionally-powered two-wheelers
Large electric two-wheelers
Large conventionally-powered two-wheelers
Battery-electric cars
Conventional passenger cars
Diesel bus
Electric rail

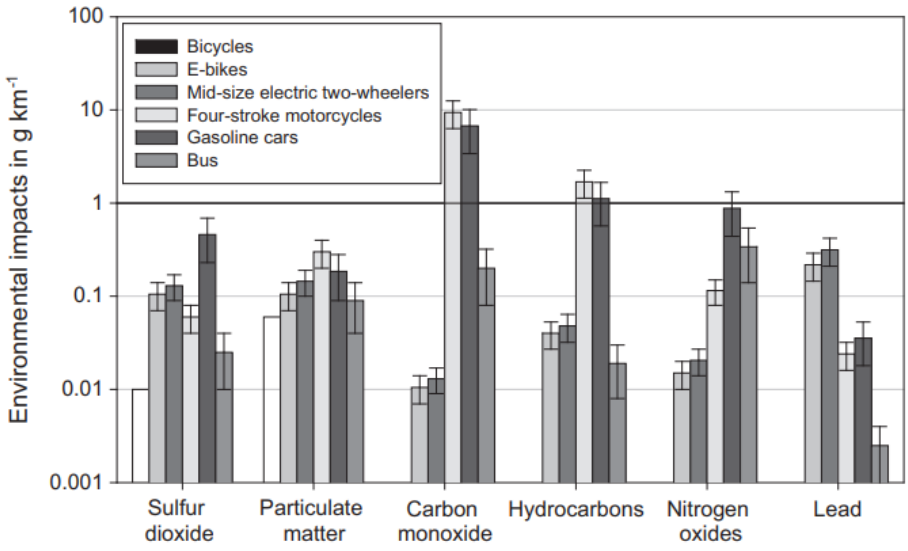

Figure 2 – Comparison of energy consumption and emissions of conventional and electric vehicles [10]

2.2 – E-bikes

As said in the previous paragraph, electric two-wheeled vehicles have become increasingly popular, with e-bikes being a particularly attractive option due to their cost-effectiveness, versatility, and safety. They represent a suitable middle ground between lighter options like scooters and heavier vehicles like motorcycles. However, there is no universal definition of an e-bike, and each country has established its own regulations for this type of vehicle.

2.2.1 – Definition of e-bike

The highest level of classification is mainly based on the type of assistance the vehicle provides: if the electric motor assists the driver only during pedaling, the vehicle is classified as "Pedal-Assist" (PAS) or "PEDal ELEctric Cycles" (Pedelecs). If the motor provides power independently of the cyclist's pedaling, the vehicle is classified as "Power-On-Demand (POD)" [11].

The first category uses the cyclist's pedaling as the control system input, and the motor provides torque proportional to the torque required by the cyclist. In the second category, the motor is controlled independently of pedaling via a throttle generally placed on the handlebars in a manner similar to classic motorcycles.

Under these two macro categories there are many possible configurations and very heterogeneous performance. To better delineate the concept of an e-bike, this paper refers to European regulations that define basic characteristics: no license is required, the motor provides assistance only while pedaling, electric power is limited to a maximum of 250 W, and the maximum speed with active motor is 25 km/h [12].

However, many models and configurations fall under this definition, but it is still possible to identify the basic components that constitute the electric powertrain of a general e-bike: an electric motor, this can have various positions and technology; a motor controller, with torque sensors and cadence sensors to respond to the cyclist's inputs; a battery pack; a user interface system; and a speed sensor [13].

2.2.2 – Electric powertrain configurations

A subsequent differentiation can be drawn based on the configuration of the electric powertrain; with regard to the illustration in Figure 3, two primary arrangements may be identified.

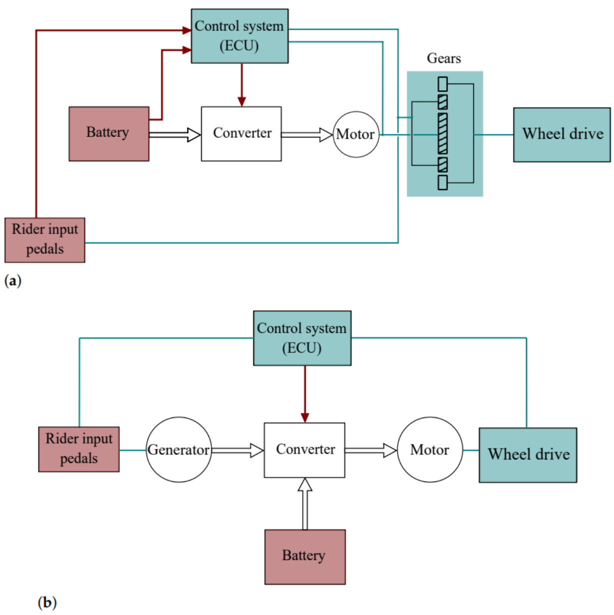

Figure 3 – (a) Parallel powertrain, (b) Series powertrain [14]

The primary type is designated as "Parallel powertrain," wherein the electric motor and rider's torque act in parallel to facilitate the movement of the vehicle, resulting in the combined torque acting upon the driving wheel. This variety is extensively employed with various modifications. Conversely, the "Series powertrain" setup is far less prevalent as it is still undergoing experimentation. A powertrain of this nature is considerably more complex: the rider is mechanically detached from the driving wheel, and the torque generated by pedaling is exclusively utilized to generate current through an electric generator. The generator's purpose is to replenish a battery that supplies power to an electric motor employed for propulsion. The pedals are thus transformed into both an energy source and a human-machine interface, as the control system interprets the pedal movement and subsequently activates the motor to maintain a natural pedaling sensation. This system has the potential to be highly efficient since the cyclist always pedals at high-efficiency operating points, independent of the bicycle's speed [15].

Figure 4 – "SeNZA" prototype: series powertrain e-bike developed by Politecnico di Milano and zeHus s.r.l.

This thesis work focuses on the Pedelecs with parallel powertrain configuration, so other categories of e-bikes are not discussed futhermore.

2.2.3 – Parallel powertrain pedelecs

The motor can be positioned in various locations, as depicted in Figure 5. Friction motors are a simple and inexpensive alternative, although they have drawbacks, including reduced power, diminished efficiency caused by excessive wear on the traction wheel due to friction, and a bigger impact on the aestethic of the vehicle due to their restricted integration capabilities.

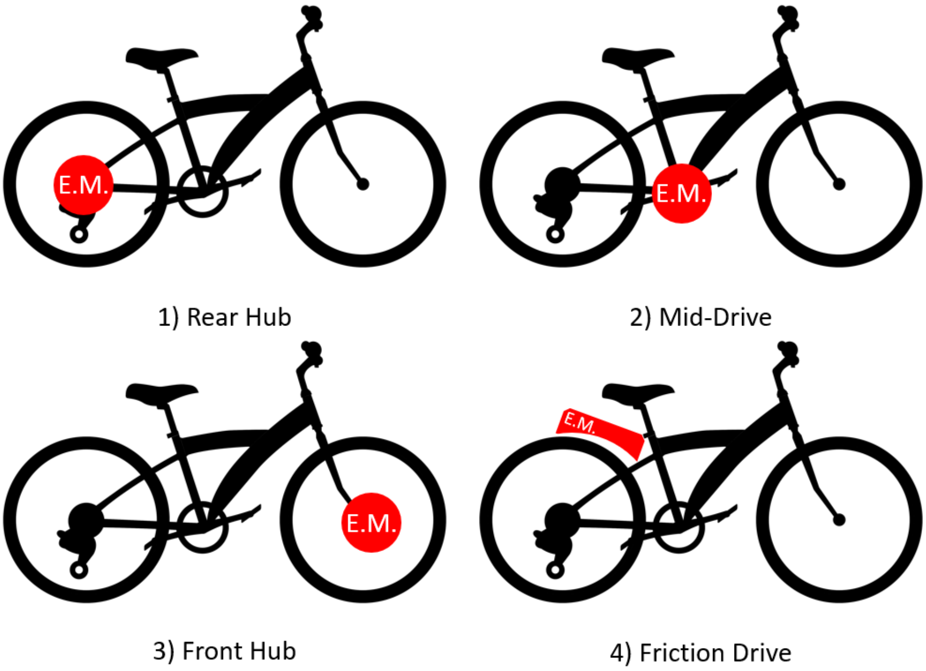

Figure 5 – Different mounting points of E.M. in e-bikes.

In contrast to friction motors, which have limitations in terms of power and integration, front-wheel and rear-wheel hub motors are popular alternatives for electric bicycles. Front-wheel hub motors offer better bike weight balance and easy installation and removal but may result in front wheel slippage, difficulty in controlling and steering, and lower power output. Rear wheel hub motors, on the other hand do not cause wheel slippage, but they may create an imbalance between the front and rear parts of the bike. Mid-drive motors, although requiring custom-designed frames for integration, offer a better weight balance, better climbing performance, and direct integration into the bike frame.

However, they are generally more expensive than hub motors of similar power [14].

2.2.4 – E-bikes market

One of the earliest e-bike prototypes was developed in the late 1800s by Ogden Bolton, an American inventor. Bolton applied a direct-current to a 6-pole electric motor to the rear hub of a bicycle and powered it with a 10-volt battery placed under the horizontal tube of the frame. The motor did not have gears to demultiplex the rotation, resulting in high torque demand and short range, as there were no pedals to assist the motor [16]. However, there is no record of any actual production of these vehicles.

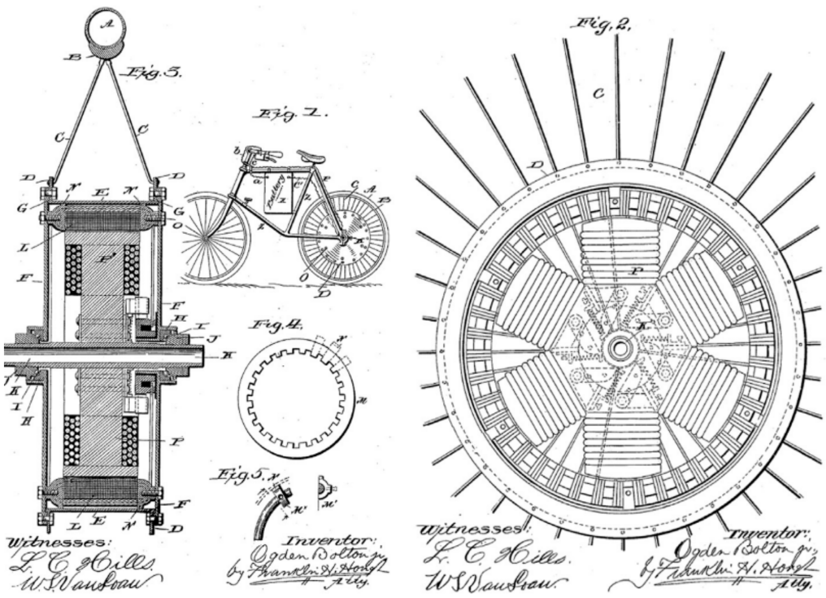

Figure 6 – One of the first e-bike prototype from Bolton [16]

The first commercial models appeared only a hundred years later [17], and since that time, e-bikes have continued to be researched and developed with increasingly advanced technologies to significantly increase their performance.

Currently, there are many models of pedelecs available with specific features for each usage scenario (Figure 7). At the state of the art, these vehicles offer greater autonomy and ease of use, allowing them to move around urban centers while reducing the problem of parking and making longer trips. They are reliable, easy to drive, convenient, and help people to live and travel a little more ecologically friendly, which greatly benefits their health [18]. They also reduce fuel consumption and pollution, helping to improve air quality and the environment. In addition, people can switch to a healthier travel solution with the convenience of reduced physical exertion [19]. Electric bicycles also provide the boost needed to travel much longer or challenging bicycle routes. Electric motor assistance helps overcome hills, inclines, and rough terrain, allowing for a smoother ride. As a result, the younger generation of cyclists is embracing this technology, making climbs less difficult and going farther and faster than they could have done with their own pedal power. In addition, this new technology helps people who could not use a traditional bicycle due to physical pain to pedal [20].

Figure 7 – Some examples of Pedelecs [21]

These are some of the factors that allowed the e-bike market a consistent growth since the early 2000s. In fact, in 2021, the e-bike market was estimated to be worth USD 17.83 billion, and it is projected to continue to grow at a compound annual growth rate (CAGR) of 13.5% from 2022 to 2030.

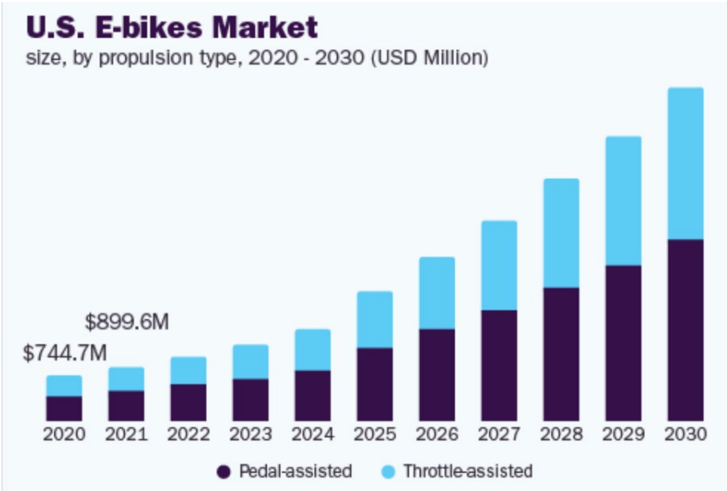

Figure 8 – E-bikes market analysis [22]

During the COVID-19 pandemic, the e-bike market experienced a temporary halt in growth in the first half of 2020 due to production suspensions. However, as the pandemic continued, people began to turn to alternative modes of transportation, leading to an increase in e-bike sales.

The Asia Pacific region is now the world leader in this market, accounting for 81% of revenue, with China alone producing 90% of the world's e-bikes.

Many major auto companies, including Ford, Honda, Peugeot, Mercedes, BMW, Volkswagen, Opel, Hyundai, Lexus, and General Motors, as well as technology companies like Bosch and Shimano, are showing interest in the e-bike industry and developing new technologies for it [13].

2.4 – The Batteries Problem

The main source of energy is the installed battery pack. In modern e-bikes the batteries can be classified in five main types [23]:

- Lead-acid
- Nickel-Cadmium (NiCd)
- Nickel-metal hydrate (NiMh)
- Lithium-ion (Li-ion)
- Lithium-ion polymer (LiPo)

The first three types of batteries have been used in the past and now rarely employed in the contest of e-bikes because of their low energy-to-volume ratio. Li-ion and LiPo batteries are ideal for use in e-bikes due to high energy efficiency, high energy-to-volume ratio, low weight and small "memory effect" compared to the other types of batteries. However, they require complex Battery Management Systems (BMS) to protect from over-heating, over-discharging and over-charging that would otherwise compromise the functionality of these devices. Moreover the price of LiPo and Li-ion batteries are considerably higher: it is estimated that lead-acid batteries cost about $35/kWh, NiMH about $350/kWh and Li-ion up to $710/kWh [13]. Furthermore, the environmental footprint for manufacturing and disposing is heavy.

In the context of e-bike application, the battery pack is generally constructed by connecting several Lithium-ion cells in series to obtain the desired voltage, typically 36 V or 48 V. The rated current is approximately 10-20 A, while during overload conditions, it can reach up to 40-50 A for a limited period. A prevalent approach nowadays is to install an integrated battery pack within the bicycle frame. The integration of batteries into the frame offers significant benefits, including enhanced durability due to protection from adverse environmental conditions such as dust, wetness, and dirt [14].

Parameter	Value	Unit
Battery voltage	36/48	V
Capacity	11–20	A h
Energy	400–750	W h
Cycle life	800–1000	cycles
Charging time w/compact charger		
	50% of the capacity	2.5–4.2 h
	100% of the capacity	6.5–8.8 h
Charging time w/standard charger		
	50% of the capacity	1.5–2.1 h
	100% of the capacity	3.5–5.4 h
Charging time w/fast charger		
	50% of the capacity	1–1.4 h
	100% of the capacity	2.5–3.7 h
Operation temperature	−20–60	°C
Weight	2.9–4.3	kg

Figure 9 – Integrated battery specifications for e-bike application [14]

Batteries represent a crucial aspect for electric vehicles (EVs), including e-bikes. Specifically, the battery pack accounts for approximately 30% of the e-bike's weight and approximately 48% of its total cost [24]. Larger batteries correspond to increased weight and costs, whereas smaller batteries result in shorter cycling range and the need for more frequent recharging.

However, implementing regenerative braking could enable reducing the battery size, and therefore the cost and weight, without compromising the e-bike's range. Alternatively, it would allow for maintaining the conventional battery size while increasing the range.

This notion is supported by Stilo et al.'s study [13], which surveyed 638 individuals on their preferred features for an e-bike. Regenerative braking was ranked absolute second among the requested "convenience features."

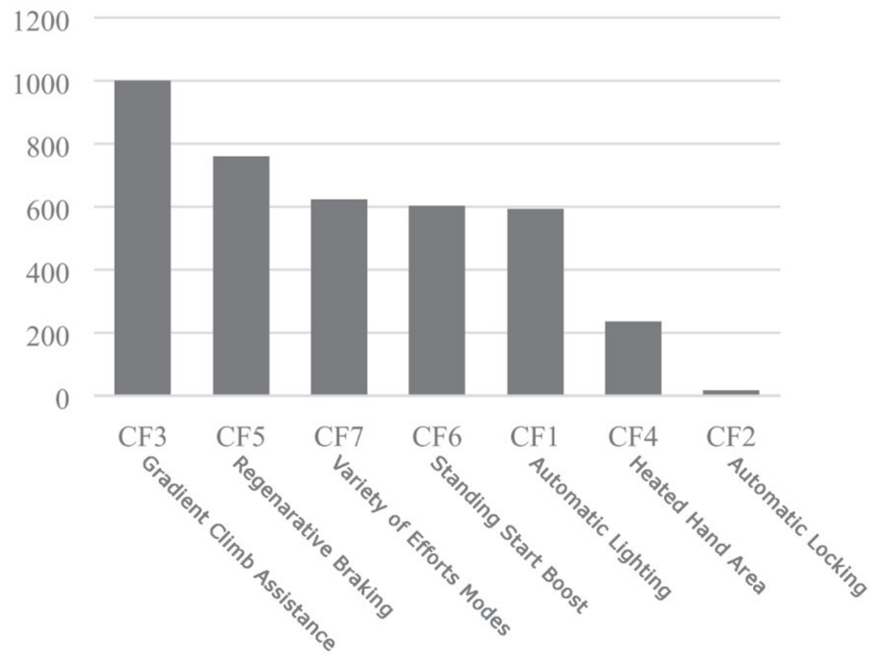

Figure 10 – Most requested e-bike convenience features [13]

Despite the potential benefits of regenerative braking, there are several drawbacks that must be considered. Firstly, a customized control system must be configured precisely to ensure that the electric braking is both responsive and safe. Additionally, the electric motor must be capable to function as a generator and the Battery Management System must account for additional current input.

The objective of this thesis is to assess the viability and potential of regenerative braking on a pedelec with a rear-hub motor. This is accomplished by developing a model and subsequently validating it through experimentation.

CHAPTER 3 – System Definition

In order to build a model to carry out useful simulations and understand the dynamics of the system, it is necessary to define, albeit in a non-final way, the mechanical and electrical configuration of the system.

This chapter discusses the choice of the various components, particularly the choice of the electrical machine, which is the heart of the entire project.

3.1 Mechanical Configuration

Decathlon r-bike (Regular Bicycle) "Rockrider ST 530 M" with 27.5'' wheels [25] was chosen as the reference model with a modification of the rear wheel that will have to be replaced with a 26'' compatible with the motor installation.

The transmission between the chainring and rear wheel is a modified Decathlon 7v. The seventh gear cannot be used because it is incompatible with later modifications of the system.

Figure 11 – Base r-bike Model.

Chainrings	32T					
Cassette	28T	24T	22T	20T	18T	16T
Tau	0.8750	0.7500	0.6875	0.6250	0.5625	0.5000

Table 1 - Drivetrain characteristics

The total weight of the vehicle thus described is 14.16 kg.

It is also necessary to consider major variations to this basic model such as the addition of support structures for battery and electrical apparatus and a modified (or additional) brake lever to control the electrical braking.

3.2 Electrical Configuration

The choice of electric powertrain will decide the capabilities and performance of the entire system. An Electric Machine that belongs to the category of Brushless Permanent Magnet Motors powered by Alternating Current (BLAC) was chosen. The choice is justified by the fact that this type has countless advantages in this field of application over other types of electric machines [26]:

1. Reliability and durability: they have no moving parts that can wear out, making them more reliable than motors with brushes.

2. Control precision: through electronic control speed and torque output can be adjusted very precisely.

3. Quiet operation: they operate more quietly than motors with brushes.

4. Versatility: they can be used both as motors and generators, a key point for the development of regenerative braking.

5. Power density: at the same size compared to other types of E.M. they deliver more torque.

3.2.1 – Electric Machine Selection

The choice of the E.M. is a key point in defining the system since, based on its characteristics, other key components such as mechanical transmission and control system are selected. In addition, the performance of the E.M. in generator mode determines the amount of recoverable energy in braking.

The machine chosen is a custom motor "NS9NM10" designed specifically for this application; this belongs to the category of Surface Mount Permanent Magnet Synchronous Machines (SM-PMSM) and should be installed in the rear wheel.

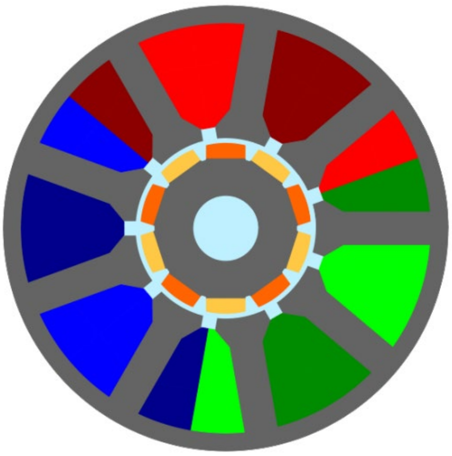

Figure 12 - Custom Motor "Ns9Nm10" Radial View in FluxMotor.

In order to build an accurate model of the system, the E.M. was characterized through laboratory tests, and the fundamental parameters of the engine were defined.

Table 2 shows the main quantities characterizing the motor; refer to the report [2] for a more detailed description.

Weight	kg	0.9308
Rotor’s Moment of Inertia	$kg * m^2$	1.421e-5
N° Poles Pairs	/	5
Stator Phase Resistances	Ω	54.28e-3
D axis Inductance	H	362.1e-6
Q axis Inductance	H	365.3e-6
Permanent Magnet Flux Linkage	Wb	10.17e-3

Table 2 – E.M. Main Parameters [2]

Generally, an Electric Machine of this type can continuously tolerate current density of $6\ \frac{A}{mm^2}$ (corresponding for this model to an RMS value of phase current of 11.781 A) and up to $20\ \frac{A}{mm^2}$ for impulsive efforts of less than 10 seconds (phase current in RMS value of 39.27 A).

These current limits result from thermal limits of the motor; too high values of current within the phases leads to overheating and consequent adverse effects on the whole system [26].

Having defined these parameters, it is possible to construct the Circle Diagram (Figure 3) [27], a useful tool for analyzing motor operating points in current-limited zones (MTPA) and voltage-limited zones

(MTPV). These considerations are analyzed more thoroughly in the next chapter, for the definition of control strategies.

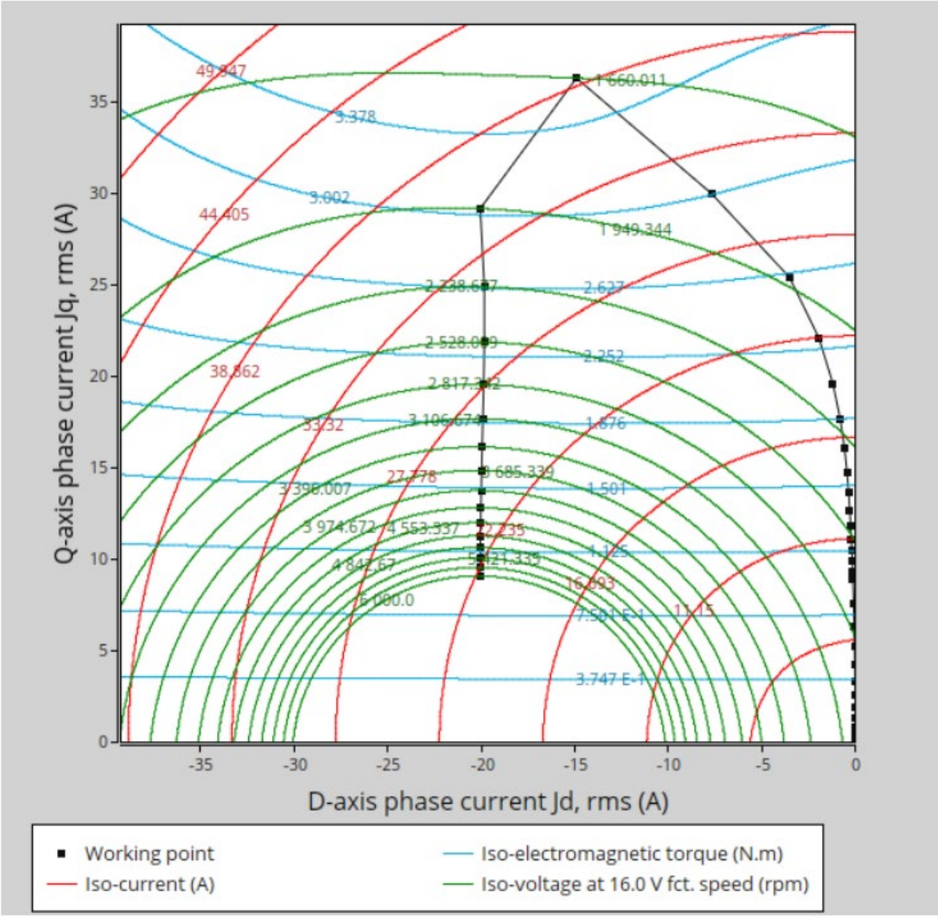

Figure 13 - Circle diagram of custom E.M.

Through characterization in the laboratory, two other important graphs are defined: Figures 4 and Figures 5 are the Torque-Speed characteristic related with Phase Current and Efficiency.

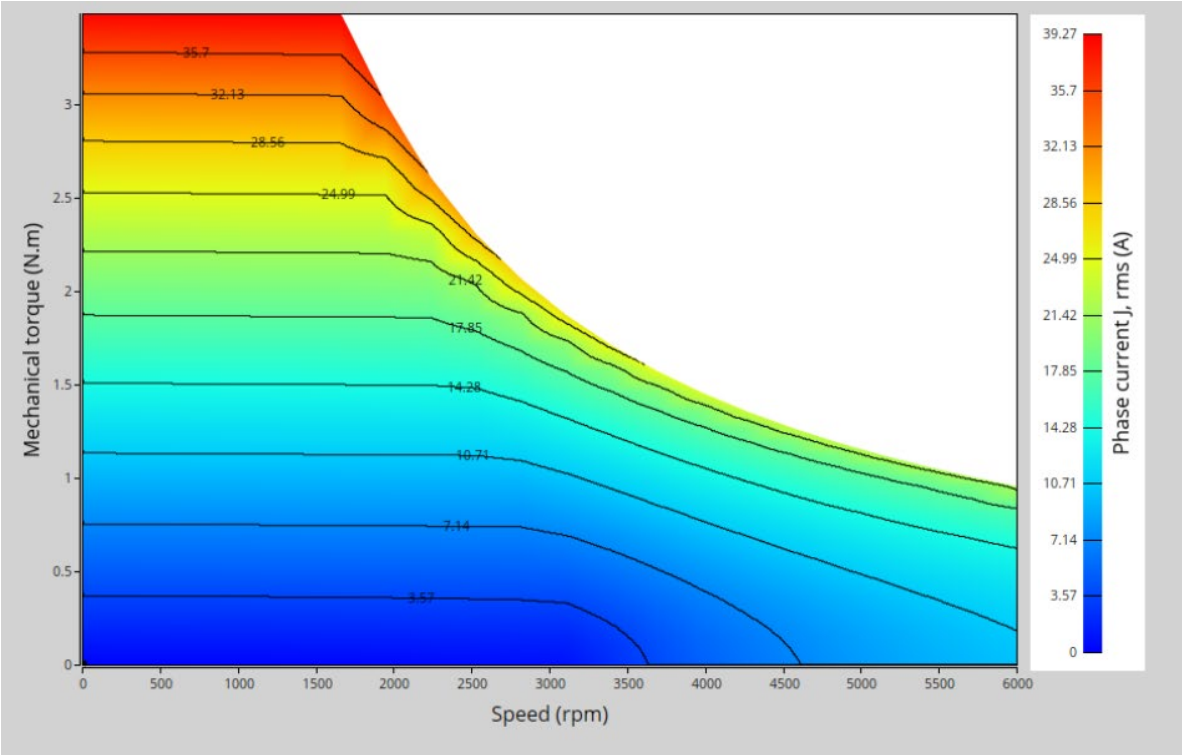

Figure 14 - Speed-Torque characteristic in relation with Phase Current

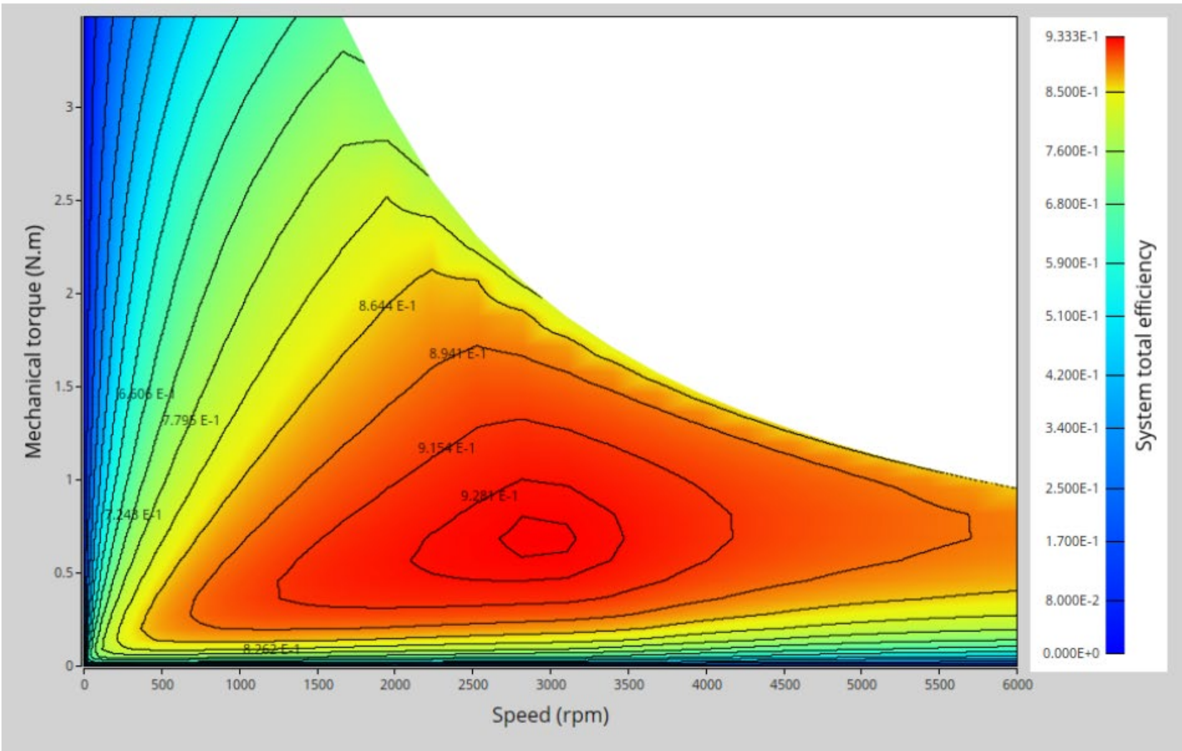

Figure 15 - Speed-Torque characteristic in relation with Efficiency

Considering the current limits, the motor can deliver up to ~1.5 Nm continuously and up to ~3 Nm for impulsive efforts; the high efficiency zone (≥90%) is found between 1500 and 4000 RPM and between 0.2 N*m and 1.5 N*m. These data are crucial for finding the desired operating points and consequently sizing the rest of the system.

3.2.2 – Additional Elements

Having defined the main characteristics of the E.M., it is necessary to define the complementary elements for the proper operation of the system. A simplified schematic of a generic control system for a PMSM is shown in Figure 6.

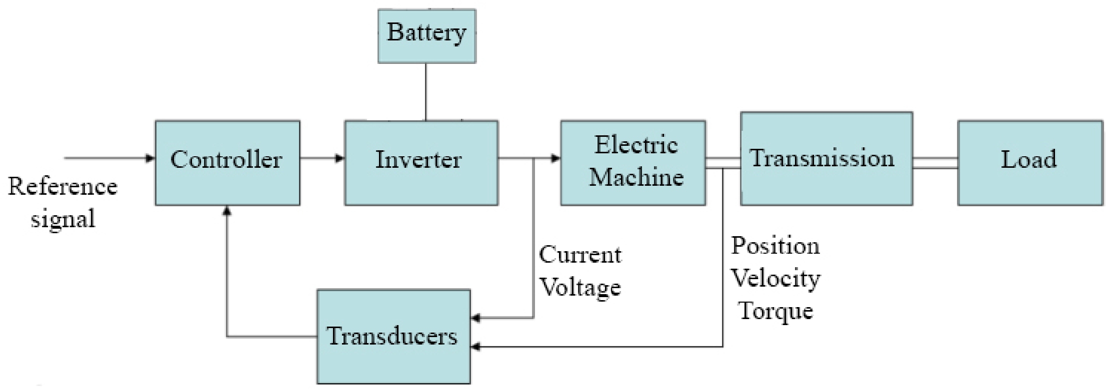

Figure 16 - Electric Drive general scheme

Fundamental elements cold be summarized in:

a) Battery
b) Inverter
c) Sensors
d) Transmission
e) Controller

a) Battery

Regarding the battery, the Cicloone 36 V 18 Ah was chosen as the reference model, which is ideal for installation on the chassis and weighs 4 kg.

The battery provides a DC voltage of 36 V while the electric machine works with sinusoidal phase voltages and therefore an Inverter block is needed.

b) Inverter

The task of the Inverter block is to receive as input a reference signal and generate as output the signal for each of the three phases connected to the motor using the output voltage from the battery. Generally in this field of application and with this type of electrical machine, the technique used to generate the phase voltages is SVPWM (Space Vector Power Width Modulation) [28], which is ideal for Field Oriented Control; this is discussed in more detail in the next chapter in the definition of control strategies.

c) Sensors

As for the sensor part, a speed and torque sensor at the pedal shaft and finally the group of sensors needed for feedback loop control of the electric motor are needed. This last group of sensors includes:

1) Absolute Encoder for calculating the angular position of the E.M.'s rotor.
2) Temperature sensor for monitoring the temperature of the motor.
3) Ammeter for measuring phase currents.

Moreover, a customized brake lever is installed on the handlebar to generate the electric and the mechanical braking signal.

In the initial phase of stroke, the lever detects an electrical signal which is subsequently processed by the control system to initiate the regenerative braking. Once a certain predetermined threshold is reached, the mechanical braking system is engaged in tandem with the electrical system to provide additional deceleration force.

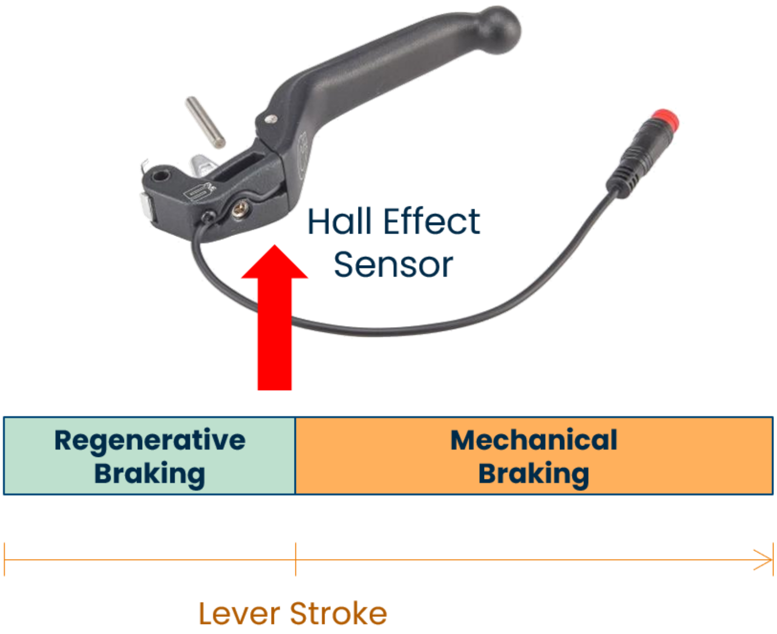

Figure 17 – Custom Brake Lever.

d) Transmission

Although an e-bike has a higher average speed than an r-bike [29], a gear ratio between the electric machine and the drive shaft of the rear wheel is strictly necessary because, as seen in Figure 15 - Speed-Torque characteristic in relation with Efficiency, the machine expresses better efficiency values for high angular speeds, far higher than average e-bike wheel's speed.

Considering that the maximum efficiency is achieved for angular speeds of about 3000 RPM and given the diameter of the rear wheel (26'' = 0.66 m), it is possible to derive the theoretical velocity of the e-bike with 1:1 transmission ratio between E.M. and drive shaft:

$$3000 * 0.66 * \pi = 6224.123 \left[\frac{m}{min}\right] = 373.44 \left[\frac{km}{h}\right]$$

Such a speed is obviously unrealistic but gives an indication of the needed gear ratio.

Considering that the average speed of an e-bike is about 17 km/h [29] a realistic gear ratio value can be obtained:

$$\frac{373.44}{17} \cong 22$$

Also considering that typically needed torques at the wheel are in the order of 100 Nm, the following gear ratio is selected in the model:

$$\frac{E.M.}{Shaft} = 30$$

e) Controller

The controller block represents a microprocessor that will manage running the algorithms for controlling the E.M. In particular, this block will have to be optimized to run Field Oriented type of control.

The configuration thus defined is named "STEP 1" and represents the basis on which the model was built, and simulations carried out.

Figure 18 - Possible "STEP 1" configuration 1) Hub E.M. + Epicycloidal Transmission 2) Battery Pack 3) E.C.U.

CHAPTER 4 – The Electric Powertrain

4.1 – The control problem

As specified in Chapter 3, a Permanent Magnet Synchronous Motor with surface permanent magnets was chosen as the heart of the powertrain. This means that the rotor is composed of laminae of ferromagnetic material on the surface of which are installed NdFeB permanent magnets that produce a magnetic field.

The stator is composed of ferromagnetic material and three phases of copper windings connected to the inverter that supplies the three-phase voltages. When the stator windings are energized a magnetic field is produced; the interaction between stator magnetic field and rotor magnetic field produces a torque. The stator is fixed to a frame, so the rotor is free to rotate, and a mechanical output is generated.

The combination of the magnetic fields produced by the three stator phases generates a rotating magnetic field [30]; in this type of E.M. the field must rotate at the same frequency as the field produced by the rotor magnets but out of phase by a certain control angle δ (-δ in generator mode). The task of the control system is, therefore, to control amplitude and frequency of this field.

Inaccuracies in generating the rotating field lead the rotor to have positive and negative alternating torque, mechanical vibration, noise, and overall poor performances and high mechanical stress.

By analyzing the dynamic behavior of the motor, the electrical equations that define the system are derived:

$$\begin{cases} v_{sa} = R_s * i_{sa}(t) + \dfrac{d\lambda_{sa}(t)}{dt} \\ v_{sb} = R_s * i_{sb}(t) + \dfrac{d\lambda_{sb}(t)}{dt} \\ v_{sc} = R_s * i_{sc}(t) + \dfrac{d\lambda_{sc}(t)}{dt} \end{cases}$$

4.1

The system of equations 4.1 defines the voltages on each phase of the stator, which are dependent on the phase currents and resistances and the flux linkage. To control instant by instant the position of the magnetic field generated by the stator, it is necessary to solve these equations which have some critical issues: although the stator resistance is constant (approximated to constant even though it is temperature-dependent), the flux linkage has a complex expression: it is dependent on current, inductances and mutual inductances, variables dependent on the instantaneous position of the rotor.

Such non-linear equations are tough to implement in a control system because they are differential equations with trigonometric terms. It is necessary to find alternative expressions to tackle the control problem more easily.

4.2 – Field Oriented Control [31]

Field Oriented Control (FOC) is a method used to control the motion of electric motors by controlling the magnetic field produced by the motor's windings.

FOC provides improved control over the motor's speed, torque, and position, which can result in higher efficiency, improved accuracy, and longer lifespan for the motor.

The main difference between FOC and other motor control techniques is that FOC uses a vector control approach. This means that it controls the magnitude and direction of the stator's magnetic field, rather than just the voltage applied to the windings. By controlling the magnetic field, FOC can more precisely control the speed, torque, and position of the motor, even under varying load conditions.

To achieve FOC, the control system must measure the motor's electrical and mechanical variables, such as the current, voltage, and speed of the motor. These measurements are used to calculate the reference currents for the motor's windings, which are then used to generate the required magnetic field. The reference currents are updated in real-time, allowing the control system to respond quickly to changes in the motor's operating conditions.

The goal of the FOC is to separately control the torque producing and magnetizing the flux components, imitating the DC motor’s operation. The electrical study of the DC motor shows that the produced torque and the flux can be independently tuned. The strength of the field excitation (the magnitude of the field excitation current) sets the value of the flux. The current through the rotor windings determines how much torque is produced. The FOC allows to decouple the torque and the magnetizing flux components of stator current. With decoupled control of the magnetization, the torque producing component of the stator flux can now be thought of as independent torque control. To decouple the torque and flux, it is necessary to engage mathematical transforms: Clarke and Park transformations.

These transformations allow the initial three-phase system to be transformed into an orthogonal system in d-q axes, rotating and fixed to the rotor with the d-axis coincident with the direction of permanent magnets’ magnetic flux direction (Figure 19 - Clarke and Park transformations).

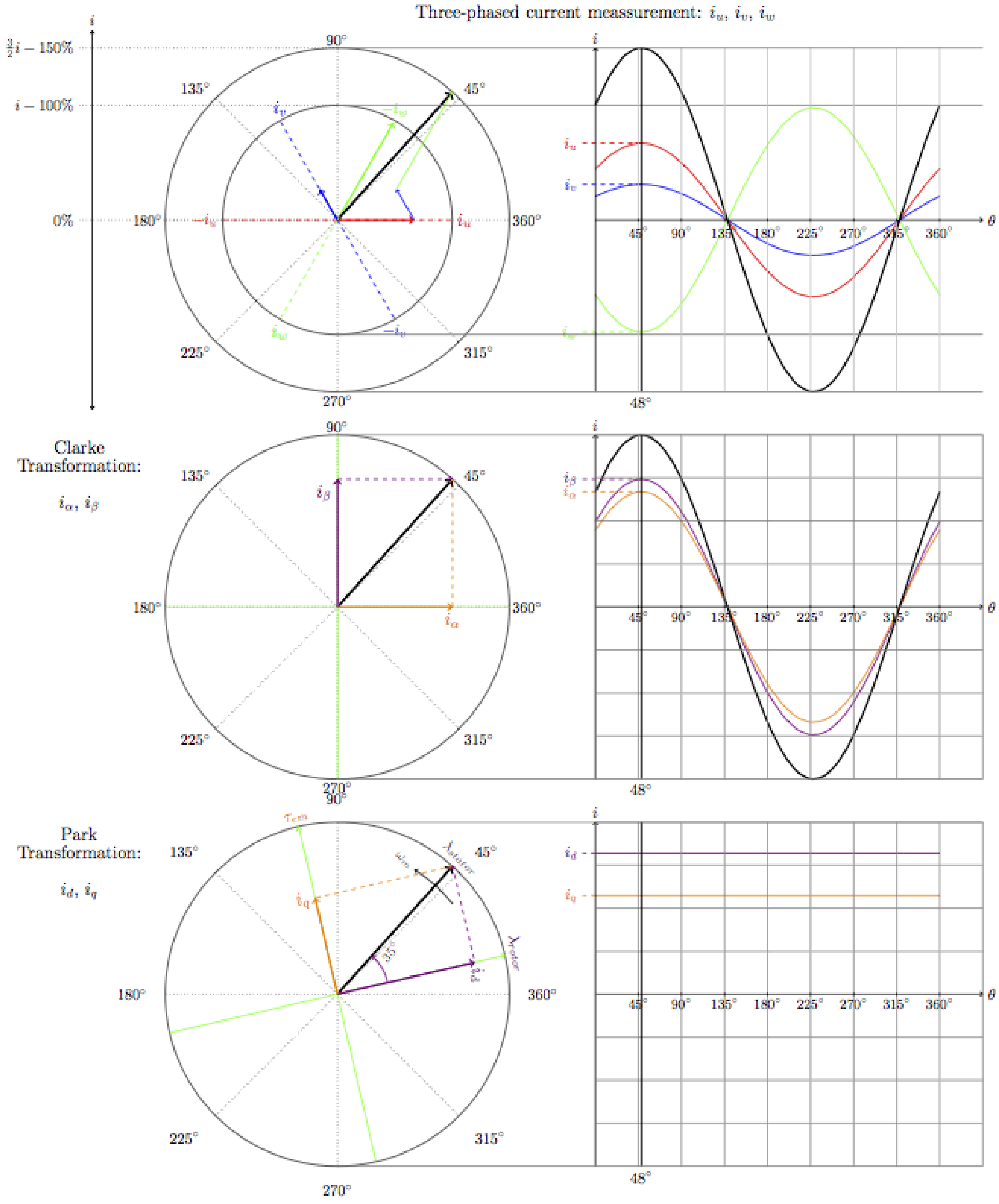

Figure 19 - Clarke and Park transformations

To control the rotating magnetic field the stator three-phase currents are measured and transformed in the rotating d-q reference system, the control process is carried out and the control voltages are generated. Inverse transformations are applied to the control voltages to generate back the three-phase voltages. The three-phase control voltages are fed to the inverter which through SVPWM techniques generates the voltages for the motor (Figure 9).

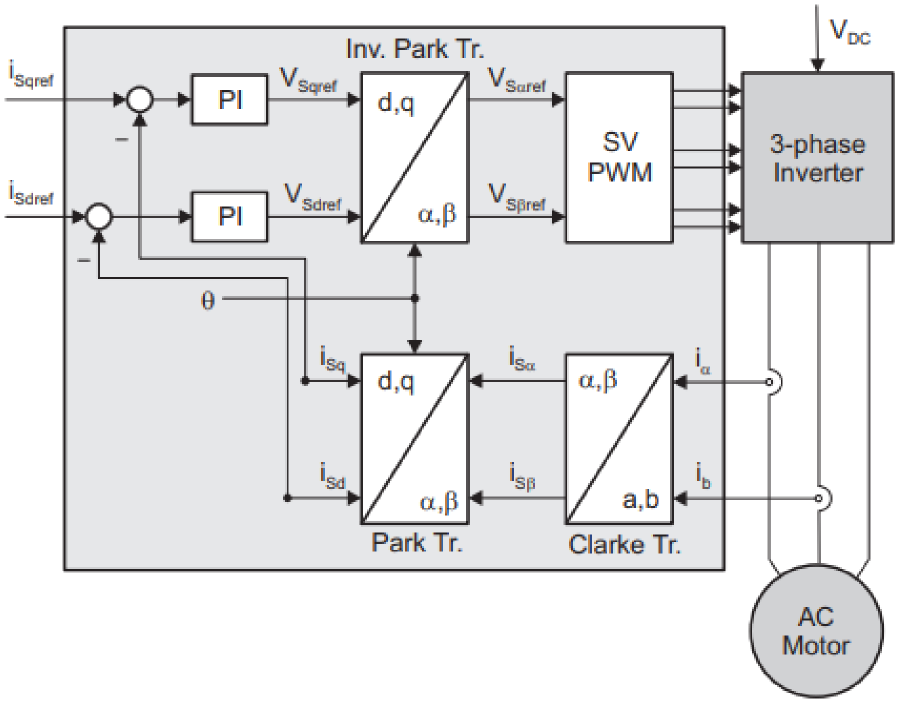

Figure 20 – Basic Scheme of FOC

To better understand this control strategy, it is necessary to analyze the characteristic equations of the system in d-q axis.

4.2.1 – System Equations in d-q Axis

It is therefore possible to completely describe the system in the new rotating reference system; the equations (4.1) characterizing the motor in a three-phase system can be rewritten as:

$$\begin{cases} v_d = R_s * i_d + L_d * \dfrac{di_d}{dt} - \omega_r * L_q * i_q \\ v_q = R_s * i_q + L_q * \dfrac{di_q}{dt} + \omega_r * L_d * i_d + \omega_r * \Psi_{pm} \end{cases}$$

4.2

Where:

- i_d = d-axis current
- i_q = q-axis current
- R_s = Phase resistance
- ω_r = Mechanical angular speed
- $Ld,\ Lq$ = d-q axes inductances
- Ψ_{pm} = Permanent magnets' magnetic flux

The first two terms in 4.2 characterize the RL circuit and represent the ohmic-inductive voltage drop, while the last term in the q-axis equation represents the back electromotive force (back EMF), which depends on the rotational speed of the machine and the flux generated by the permanent magnet.

The third term in both equations is called the "coupling term" because it represents the influence of one axis with the other. The presence of this term is justified by the fact that although the two axes are in quadrature, they are actually derived from a mathematical representation of the physical system that involves three windings that are 120° out of phase and therefore are not physically decoupled [26].

In the control chain it is preferable that varying the voltage v_d varies only the i_d current and varying the voltage v_q varies only the i_q current so that the dynamics of the i_d and i_q currents can be controlled independently. Therefore, a control action suitable for decoupling the dynamics of the two axes is always implemented within the control system: it is supplied an equal but opposite voltage in the control chain to eliminate that contribution.

The set of equations to describe the dynamic behavior of the motor in d-q axes is complete with the electromechanical torque equation [32]:

$$C_e = \frac{3}{2} * n_p * \left(L_d - L_q\right) * I_m^2 * \frac{\sin(2 * \delta)}{2} + \frac{3}{2} * n_p * \Psi_{pm} * I_m * \sin(\delta)$$

4.3

Where:

- I_m = Magnitude of current vector in d-q plane
- n_p = Number of poles
- $Ld,\ Lq$ = d-q axes inductances
- Ψ_{pm} = Permanent magnets' magnetic flux
- δ = Control angle (fig. 10)

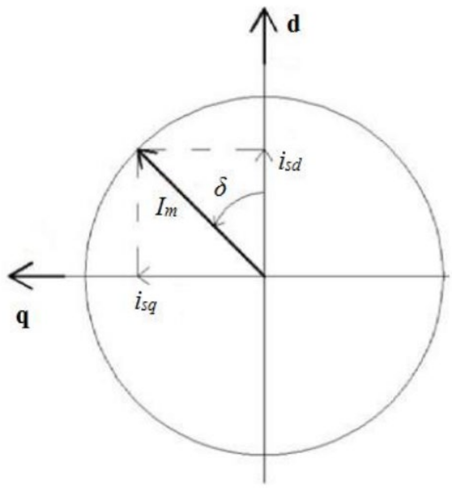

Figure 21 - Current Vector in d-q Plane

The first term in 4.3 is called Reluctance Torque and depends on both components of the current vector and the difference in inductance between the two axes (magnetic anisotropy). The second term is called Synchronous Torque and, more importantly, depends only on the q-axis component of the current vector.

In an ideal Surface Mount PMSM the inductances in d and q axes are exactly equal, the Reluctance Torque term disappears, and maximum torque is obtained by shifting the current vector completely to q-axis, i.e. for $\delta=\pi/2$. In that case we speak of maximum torque per ampere (MTPA) control that will be more deeply discussed later.

In the real case the inductances Ld and Lq are not perfectly equal (Table 2) therefore the Reluctance Torque does not disappear completely though still negligible having the difference in inductances in the order of $3 * 10^{-6}$. The anisotropy of the machine will slightly shift the control angle for the MTPA strategy (Figure 22).

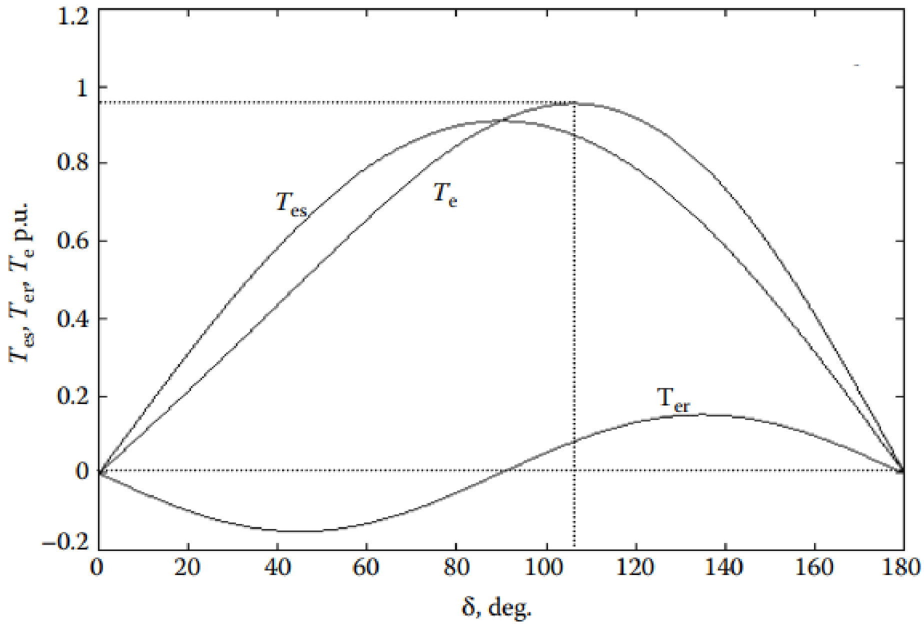

Figure 22 - Reluctance Torque (Ter), Synchronous Torque (Tes) and Effective Torque (Te) for an Anisotropic Machine.

4.2.2 – Torque Control

To build the control system, it must be considered that the motor will have as an external input an angular velocity given by the fact that the motor is mechanically connected to the rear wheel. Therefore, the control system must deal with the torque delivered by the motor and not its speed, which, however, will play an important role in controlling the motor.

Considering that the difference in inductances Ld and Lq is negligible, equations 4.2 and 4.3 can be rewritten in steady-state and ignoring the Joule losses [33]:

$$\begin{cases} v_d = -\omega_r * L_q * i_q \\ v_q = \omega_r * L_d * i_d + \omega_r * \Psi_{pm} \\ C_e = \dfrac{3}{2} * n_p * \Psi_{pm} * i_q \end{cases}$$

4.4

As discussed in [27] and [33], it is possible to define the circle diagram, a useful tool to understand torque control optimization. The phase current limit (imposed by thermal limitations for the motor) defines a circle in the d-q plane:

$$i_{ph}^2 = i_d^2 + i_q^2 \leq I_m^2$$

4.5

where:

- $I_m = \sqrt{2} * I_{rms}$ = Peak current
- I_{ph} = Phase current

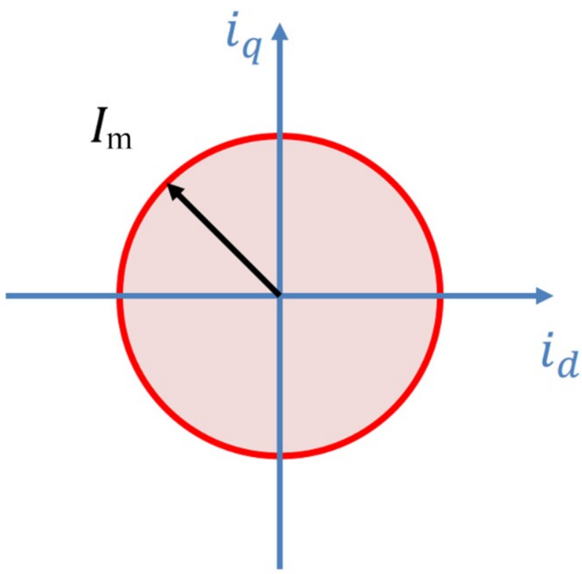

Figure 23 – Current Limited Region [33].

The limitations given by the maximum available voltage, i.e., the supply voltage of the inverter, are now considered.

$$v_{ph}^2 = v_d^2 + v_q^2 \leq V_{pk}^2$$

4.6

Where:

- v_{ph} = Phase Voltage
- $V_{pk} = \frac{V_{dc}}{\sqrt{3}}$ = Peak voltage for SVPWM Inverters [28]

Using 4.4 and 4.6 the expression of the voltage limited region is computed:

$$\left(\xi * i_q\right)^2 + \left(i_d + \frac{\Psi_{pm}}{L_d}\right)^2 \leq \left(\frac{V_{pk}}{p * L_d * \omega_r}\right)^2$$

4.7

Where:

- $\xi = \frac{L_q}{L_d}$ = Saliency ratio

Equation 4.7 represents an ellipse in the d-q plane. For a magnetically isotropic motor, i.e. $\xi \cong 1$, the ellipse degenerate into a circle.

The center of the ellipses is defined by the constitutive parameters of the motor, while the area is directly proportional to the supply voltage and inversely proportional to the angular speed (Figure 24).

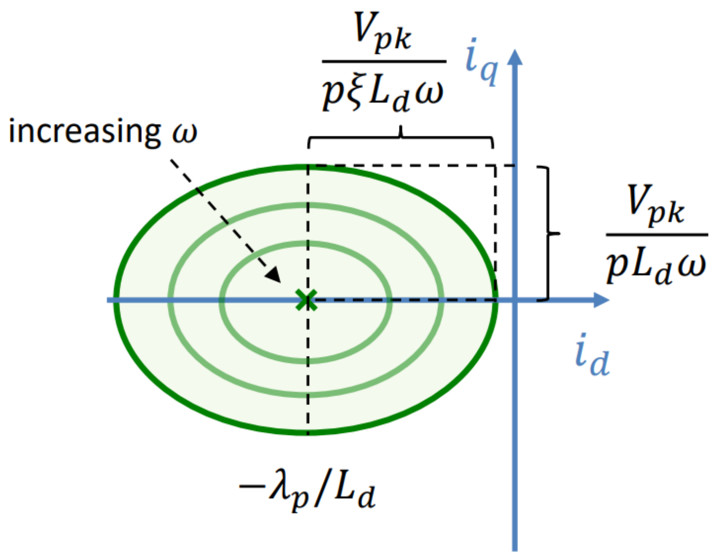

Figure 24 – Voltage Limited Region [33].

Using the third equation in 4.4 it is possible to define torque isocurves. The expression is shaped to have i_q in function of i_d:

$$i_q = 2 * \frac{T}{3 * n_p * \left(\Psi_{pm} - (\xi - 1) * L_d * i_d\right)}$$

4.8

Equation 4.8 represents a hyperbola in the d-q plane however, again due to the isotropy of the machine, this expression degenerates into a straight horizontal line.

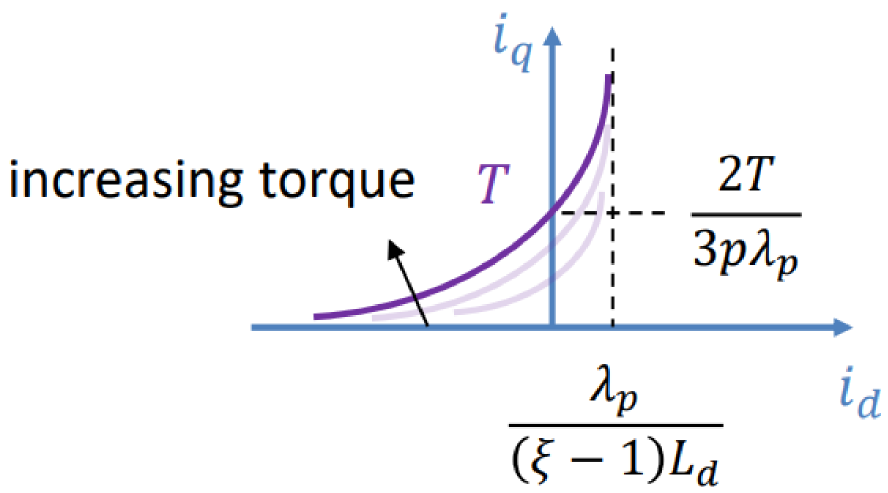

Figure 25 – Torque Isocurves [33].

As observed, up to a certain size of the voltage limited region, i.e., up to a certain motor speed, controlling the magnitude of the vector i_q suffices to regulate the delivered torque. The peak torque is achieved when the current vector I_m aligns with the q-axis. This point is referred to as the Base Speed Point.

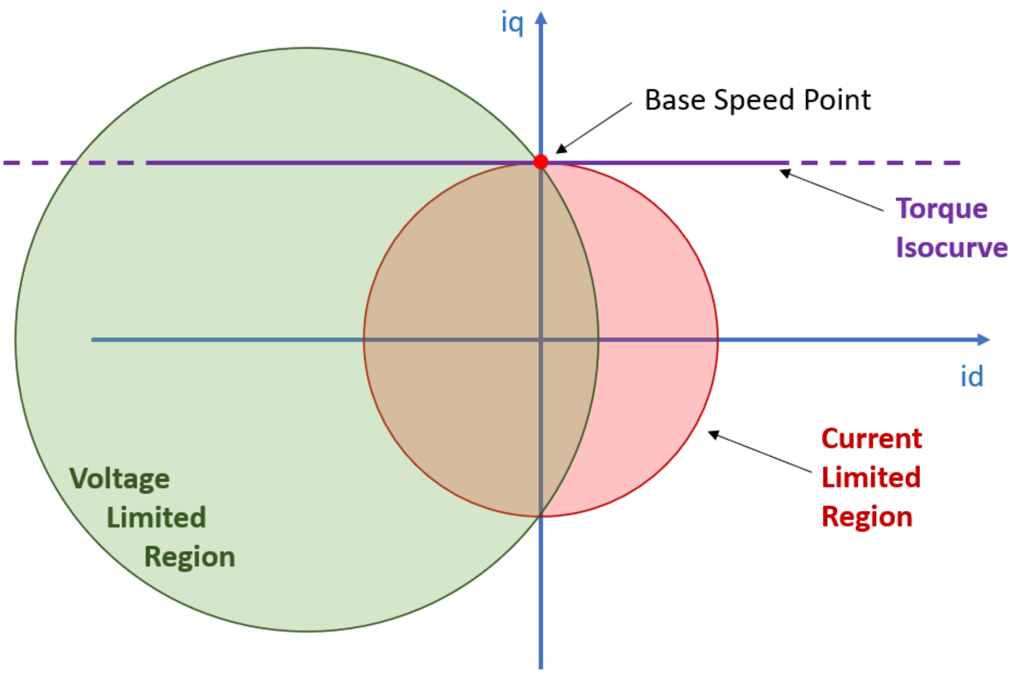

Figure 26 – Current limited region, voltage limited region, torque isocurve and base speed point for a SMPMSM.

Manipulating the equation 4.7, the expression of the base speed is computed:

$$\omega_{base} = \frac{1}{n_p} \frac{V_{pk}}{\sqrt{(L_d * i_q)^2 + (L_d * i_d + \Psi_{pm})^2}}$$

4.9

In the present case, the current i_d is zero at the base speed point.

Below that speed, the control system must handle only the current i_q for torque control however, above that speed, the motor enters the field-weakening region [27].

Over the base speed, the effect of the back-EMF is no longer negligible; therefore, the control system must mitigate the strength of the magnetic field produced by the permanent magnets by using a negative i_d current that will produce an opposing magnetic field.

The control problem of a synchronous machine became akin to the control problem of a DC machine: the current i_q corresponds to the armature current of the DC machine while the i_d component represents the excitation current that allows the magnetization level of the machine to be varied.

Coming back to the circle diagram, as the angular speed increases, the operating point moves along the circle of the current limited region following the intersections with the voltage limited region which decreases with the increasing speed (Figure 27, operating points P1, P2, P3, ...). The modulus of the vector I_m must remain constant so as the i_d component increases, the i_q component decreases and consequently the torque that the motor can express.

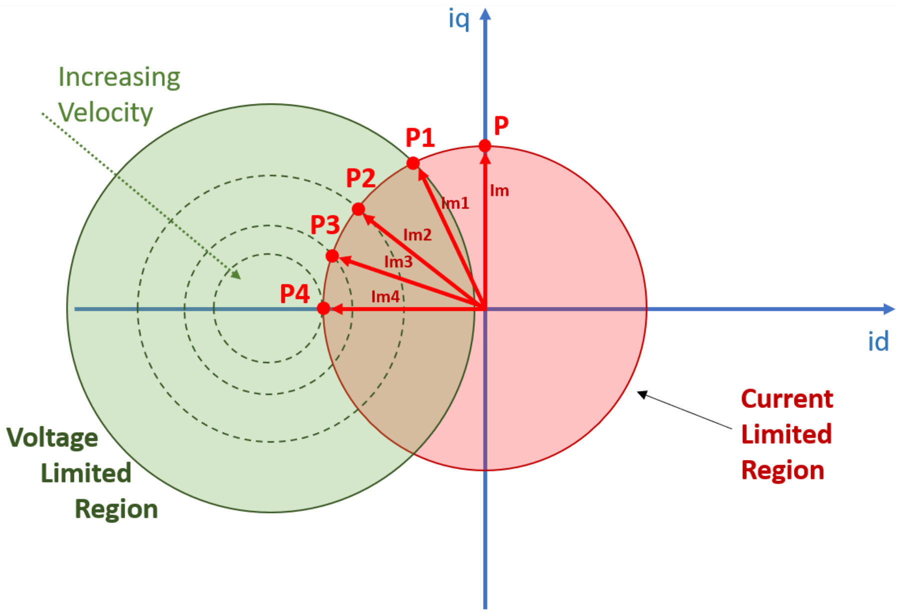

Figure 27 – Finite speed PMSM configuration.

Figure 27 represents the circle diagram of a finite-speed PMSM since the limit point is represented by point P4 at which the motor reaches limit speed and zero torque. The limit speed can be computed using 4.9 and setting $I_m = i_d, i_q = 0$.

However, although the center of the circles of the voltage limited regions is determined by the constitutive parameters of the motor, the current limited region is determined by the phase current limit. This limit is not fixed during motor operation but varies with motor temperature. For a higher maximum current limit, the operation could change from finite-speed to infinite-speed configuration, in which the motor reaches zero torque for infinite speed (point P5 in Figure 28). In that case the center of the voltage limit circles is inside the current limit circle.

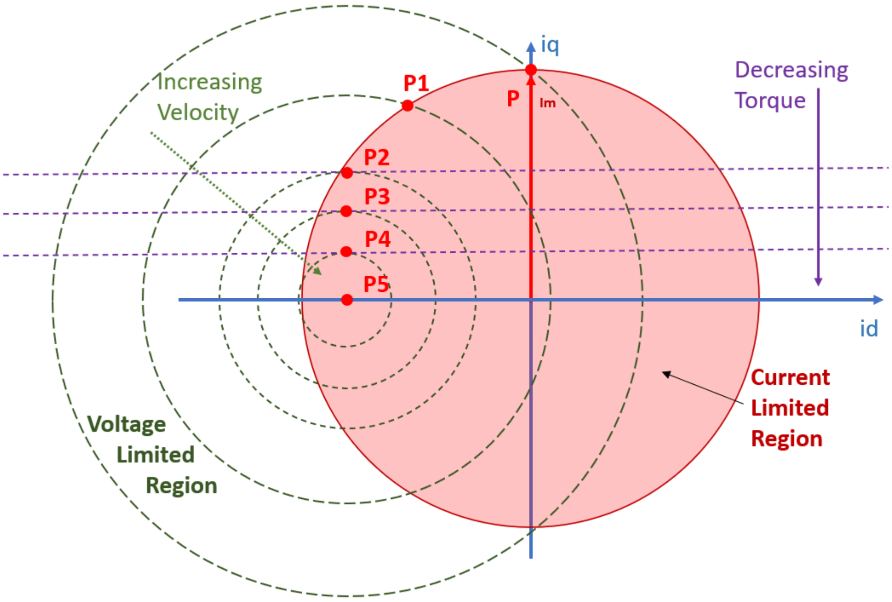

Figure 28 – Infinite-speed PMSM configuration

Having discussed the principles behind FOC, a model of the motor and the control system are built in MATLAB Simulink.

4.3 – Control System Simulink Model

The "Interior PMSM" block [34] was used to model the behavior of the motor in Simulink. This block was chosen to consider the slight anisotropy of the machine, since the "Surface Mount PMSM" block does not allow for different inductances in d-q axes.

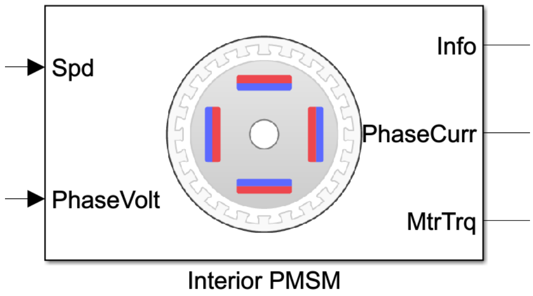

Figure 29 – Simulink block to model the motor.

To the left of the block are the inputs: Speed and Three-phase Voltages. The speed depends on the linear speed of the vehicle, which is transformed by the rear wheel and gear ratio into the angular speed of the motor. The voltages are the control input of the motor and are generated by the control system.

On the right side of the block is the "info" bus where all the fundamental variables of the motor are contained, the "MtrTrq" signal which represents the mechanical torque produced by the motor, and finally the "PhaseCurr" bus which collects the phase currents of the motor.

To model mechanical inefficiencies, a viscous damping coefficient of 4.924e-4 N·m/(rad/s) is selected in the parameter box.

4.3.1 – Motor Currents Model

Using "PhaseCurr" and the motor position (obtained by integrating the speed), Clarke and Park transformations are performed to calculate the i_d and i_q currents needed for the feedback-loop control. The currents thus calculated are also used to calculate the I_{bus} current, which represents the current at the battery level. Currents i_d and i_q are multiplied respectively by the voltages v_d and v_q and then summed. The result is multiplied by factor $\frac{3}{2}$ to obtain the d-q instantaneous power and then divided by the battery voltage (variable with the SoC and taken from the battery model) to compute the battery current (Figure 30 – Simulink model for currents $\mathrm{i_d}$, $\mathrm{i_q}$ and $\mathrm{I_{bus}}$).

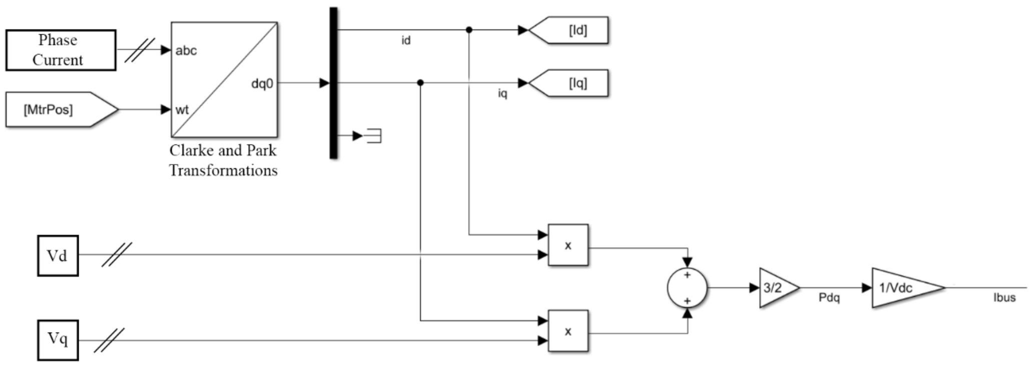

Figure 30 – Simulink model for currents i_d, i_q and I_{bus}

4.3.2 – Control System Model

In Figure 34 the control system that generates the motor reference voltages is represented. The input of the control chain is the reference torque T_{ref} and the motor speed ω_{fb}. As discussed above, the motor speed is proportional to the vehicle speed, while the reference torque is a function of the torque required by the rider. How the reference torque is generated is discussed in the next chapter.

The generation of reference currents i_{d_ref} and i_{q_ref} is achieved by using Look Up Tables (LUT) that enable the optimal control of the electric motor using the criteria discussed in section 4.2.2 – Torque Control. The electric machine is firstly modeled in software environment FluxMotor [35] that relies on Finite Elements Methods to evaluate the behavior of all variables of the motor during operations. Through these simulations, optimal i_d and i_q currents are computed for different operating points defined by torque and speed of the motor and 2-Dimensional LUTs are created. Moreover, a 1-D LUT is created to create the limit region, highlighted in Figure 31 – Iq 2-D LUT (Color Map) and Limit Region LUT (Dashed Line) and Figure 32 – Id 2-D LUT (Color Map) and Limit Region LUT (Dashed Line). Notably, the maps are generated considering the available voltage 8% less than the actual value to allow the control system to compensate Back-EMF and coupling terms even near the limit of the working region.

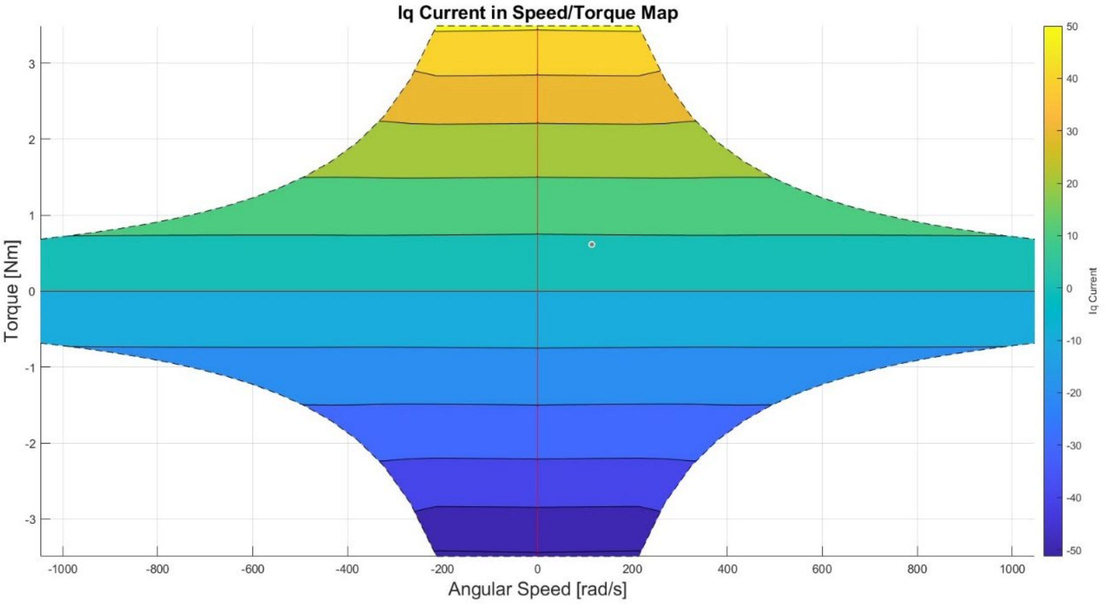

Figure 31 – Iq 2-D LUT (Color Map) and Limit Region LUT (Dashed Line).

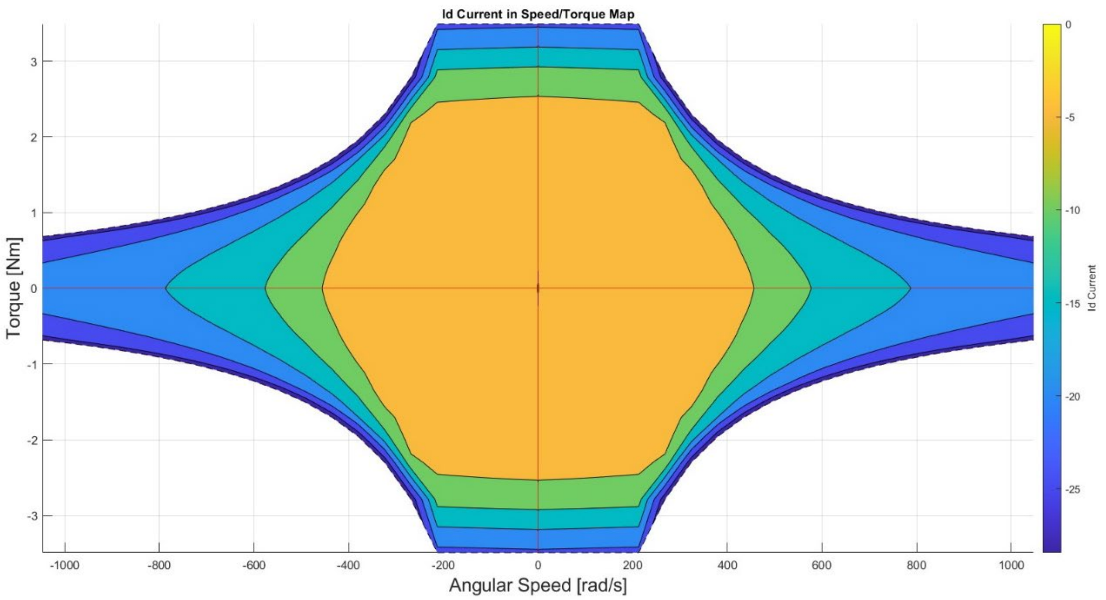

Figure 32 – Id 2-D LUT (Color Map) and Limit Region LUT (Dashed Line).

Hence, the variables T_{ref} and ω_{fb} are the input the "LUT Block" that contains the above-described maps and is schematized in Figure 33 – LUT Block Schematic. Before the deployment in the model, all the maps are set to be interpolated with the Akima Spline method to cover the whole spectrum of operating points and then tuned to avoid discontinuity points that would cause instability in the feedback-loop control.

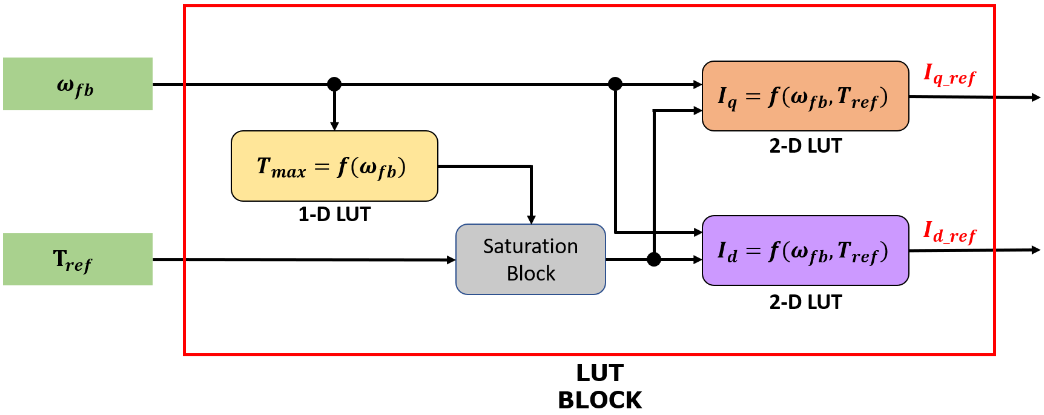

Figure 33 – LUT Block Schematic.

Once the reference currents are generated, they are compared with the feedback-loop currents generated with the model described in 4.3.1 – Motor Currents Model, and an ideal Proportional-Integrative control is implemented. The proportional-integrative gain is calculated by referring to [36]:

d-axis:

$$P_d = 2 * \pi * f_{bw} * L_d$$

$$I_d = \frac{R_s}{L_d}$$

4.10

q-axis:

$$P_q = 2 * \pi * f_{bw} * L_q$$

$$I_q = \frac{R_s}{L_q}$$

4.11

Where:

- f_{bw} = Bandwidth of the motor = 200 Hz

The PI control generates the voltages v_d' and v_q' which are corrected with the d-q axis decoupling terms and the back-EMF voltage (4.2.1 – System Equations in d-q Axis).

The next block "DQ limiter" is needed to limit the control voltage relatively to the maximum available voltage. Considering that the battery generates the three-phase voltages through SVPWM techniques, the maximum available voltage is $\frac{V_{battery}}{\sqrt{3}}$.

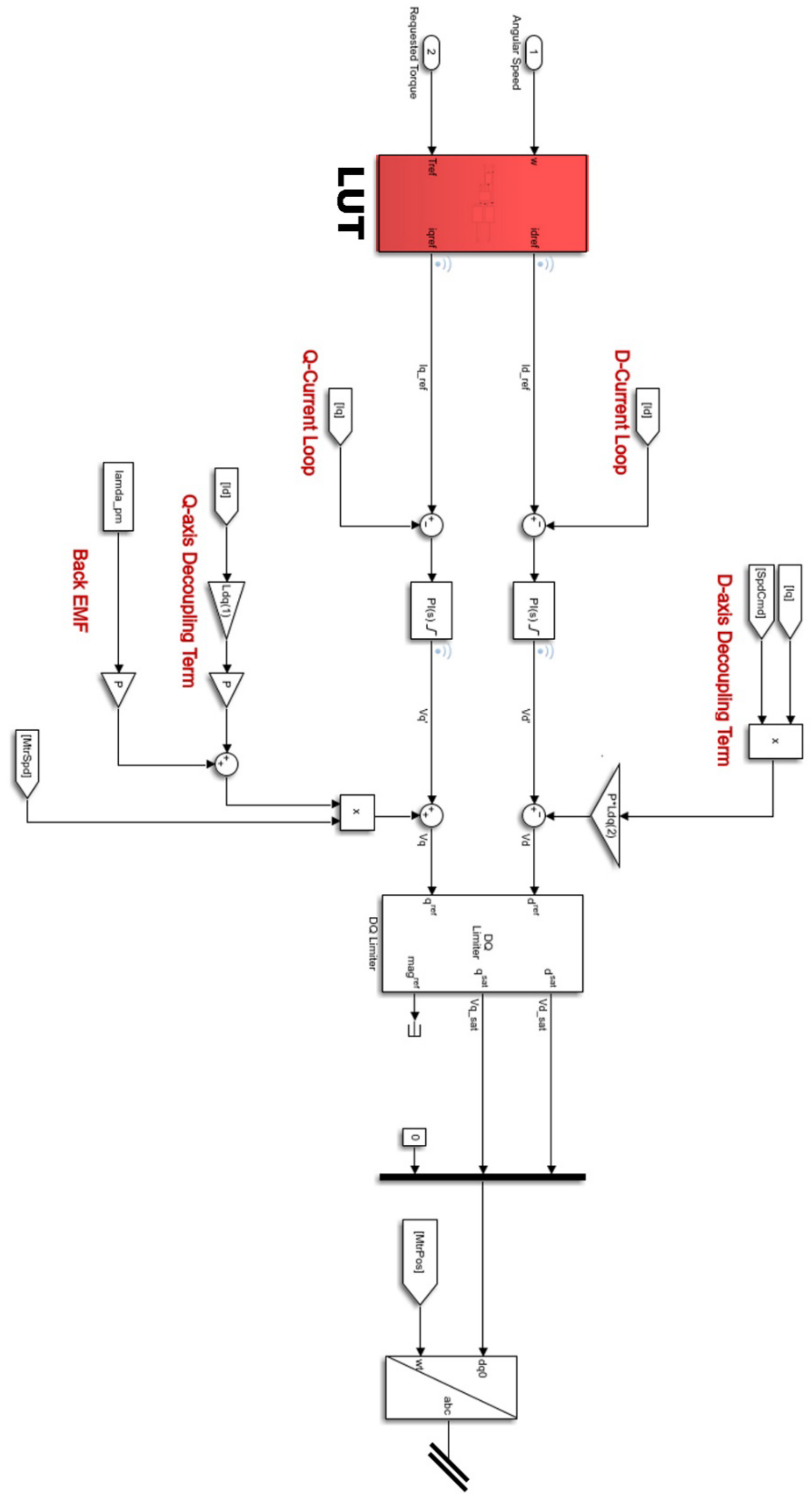

Figure 34 – Control System Model

4.3.3 – Battery Model

To model the battery behavior the "Datasheet Battery" block is used. The block is configured with 18 Ah capacity and 36 V at 100% SoC (State of Charge) to match the battery selected in section 3.2.2 – Additional Elements.

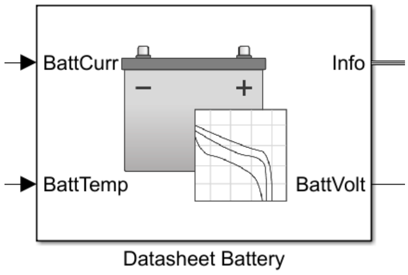

Figure 35 – Simulink Battery Block.

The inputs are "BattCurr" which represents the drained current and "BattTemp" which represents the working temperature of the battery. The "BattCurr" signal is fed with the current computed in model and the temperature is set constant at 20°.

Outputs of the block are: "Info" bus where important variables (such as the SoC) are stored and "BattVolt" that represent the voltage of the battery, function of the SoC [37].

4.4 – Electric System Efficiencies

In the preceding paragraphs, all system elements have been described and it has been identified that the electric motor model is the only source of inefficiencies having Inertia and Viscous Friction parameters. However, to develop a model that provides realistic results, it is essential to incorporate additional inefficiencies into the system. This step is imperative as there is no block in the model that represents the Inverter component or the Battery Management System component, which are critical sources of inefficiencies that must be accounted for in the system's energy balance. The battery model outlined earlier is insufficient for modeling power exchange inefficiencies, and therefore, the electrical efficiency of the system must be determined as follows:

$$\eta_{elec} = 0.85$$

The aforementioned value serves as a regulator for the efficiency of the current flowing into and out of the battery. It was selected based on an analysis of comparable systems to the one being described, and is hence deemed a realistic and appropriate value.

CHAPTER 5 – Dynamic Model

In order to assess the performance of the electric powertrain deployed in a combined cyclist and e-bike system, it is essential to enhance the existing model presented in the preceding chapter by incorporating additional blocks that simulate the dynamic behavior of the entire system.

The electrical machine and control system introduced in Chapter 4 are contained within an "E.M." block, which receives a torque reference T_{ref} and the rotor's angular velocity ω_{fb}, which is a function of the vehicle's linear velocity, as input. The primary output of the block is the mechanical torque generated by the motor, denoted by "$MtrTrq$". Naturally, all motor variables can be logged using this block. Figure 36 depicts the E.M. block in Simulink, which also provides the battery state of charge "SoC" as output. This parameter is utilized to dynamically determine the power split, a topic that will be thoroughly discussed in this chapter.

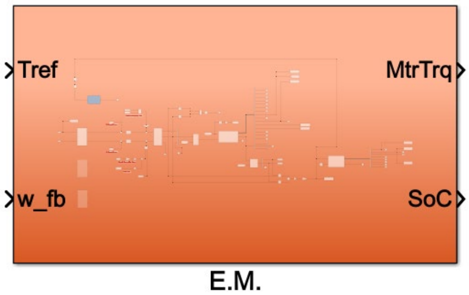

Figure 36 – Electric Machine and Control System Block.

The dynamic behavior of electric bicycles is determined not only by the motor design, control system, and battery type but also by operating conditions such as wind speed, road slope, and rider weight, as well as design parameters such as structural features (e.g., frame, wheel size, bike weight).

Consequently, to optimize the performance of the electrical system, it is necessary to include sections in the model that simulate these factors. The model is designed to process experimental data created from several routes that provide information on speed, altitude, and distance covered.

5.1 – Longitudinal Dynamic

At a macroscopic level, the dynamic of the system is modeled by considering the vehicle's longitudinal dynamics. This section is built by treating the bicycle and cyclist as a single body with a combined mass of m_{tot}, and only forces acting longitudinally on the vehicle are considered.

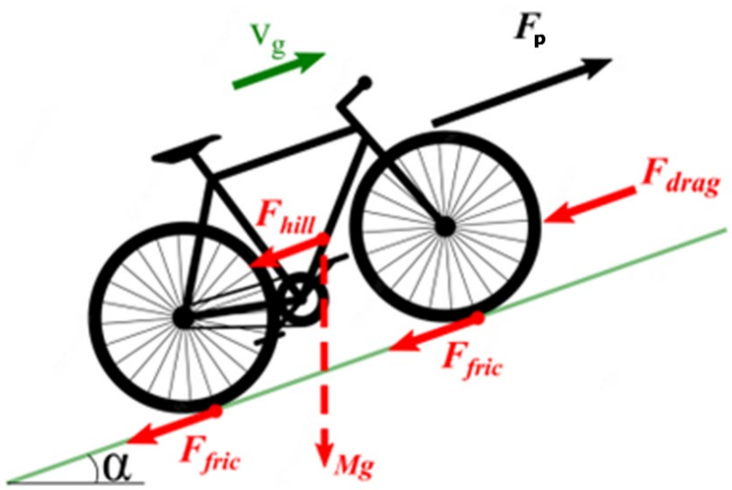

Figure 37 – Main Forces in Longitudinal Model [14].

The main forces acting on the system are defined:

- F_{drag} = Wind Drag
- F_{fric} = Rolling Friction
- F_{hill} = Gravity
- Inertia
- F_p = Propulsion Force

Wind Drag

The wind drag depends on factors related to the air proprieties, velocity and geometry of the system [38].

It is expressed as:

$$F_{drag} = \frac{1}{2} * C_d * \rho * A * v_r^2$$

5.12

Where:

- C_d = Drag Coefficient
- ρ = Air Density
- A = Frontal Area
- v_r = Relative Speed in Air

The drag coefficient is determined experimentally and typically ranges between 0.7 and 1 for an average cyclist and bicycle system [39]. The air density is a function of altitude above sea level, while the frontal area is determined experimentally by examining the system's geometries. Air drag is proportional to the frontal area of the system, hence to minimize this loss, it is advisable to integrate the additional electric component in the bike’s frame or behind the wind shield constituted by the rider. Moreover, this force is proportional to the square of the speed relative to the air, which is calculated as the sum of the vehicle's ground speed and the wind speed:

$$v_r = v_g + v_w$$

5.13

For high relative velocities this force became relevant in the equilibrium equation.

Rolling Friction

The forces produced by the rolling friction is expressed as:

$$F_{fric} = \mu * m_{tot} * g * \cos(\alpha)$$

5.14

Where:

- μ = Rolling Friction Coefficient
- g = 9.807 = Gravity Acceleration
- α = Road Slope Angle

The coefficient μ is dependent on the total weight of the vehicle, the type of bearings, and the type of tires. To determine the appropriate coefficient to run the simulations, reference was made to the research conducted by Morchin and Oman [39], where friction coefficients were measured for various bicycle categories as illustrated in Figure 38 - Rolling Coefficient Related to Total Weight for Different Types of

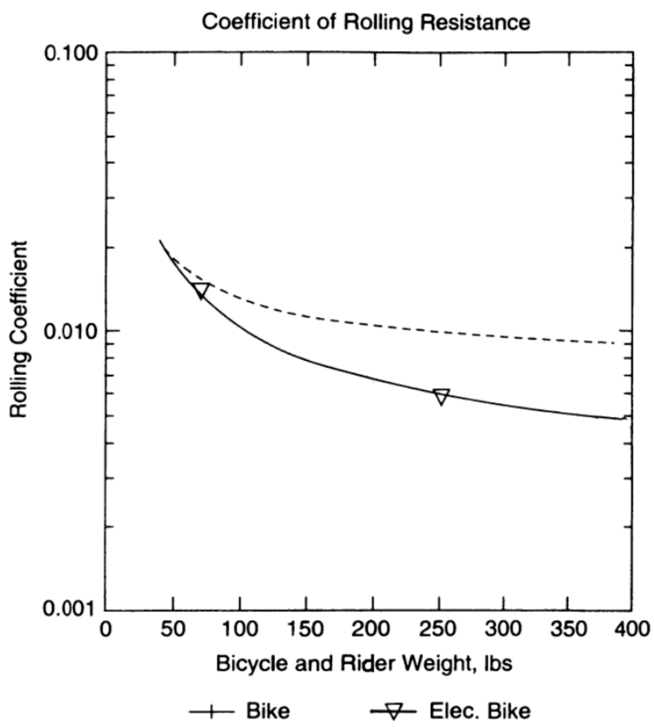

Figure 38 - Rolling Coefficient Related to Total Weight for Different Types of Bikes.

Inertia

Inertia of the system is computed as:

$$F_{in} = m_{tot} * a$$

5.15

Being a the acceleration of the system relative to ground.

Inertia of other components such as wheels and transmissions, being negligible compared to the other quantities, is neglected in this model.

Gravity

When the road slope is non-zero, a force component resulting from gravity is introduced. This force can be resistive when the vehicle is travelling uphill and propulsive when travelling downhill. In either scenario, it represents the most challenging force for the electric powertrain to overcome. This force is computed as follows:

$$F_{hill} = m_{tot} * g * \sin(\alpha)$$

5.16

5.1.1 – Dynamic Equilibrium of the System

Once described the main forces acting on the system it is possible to build the longitudinal equilibrium equation:

$$F_p - F_{hill} - F_{fric} - F_{drag} = F_{in}$$

5.17

Using this relationship, the instantaneous velocity of the system is computed and used as a feedback variable. The detailed functioning of the system is discussed later in this chapter.

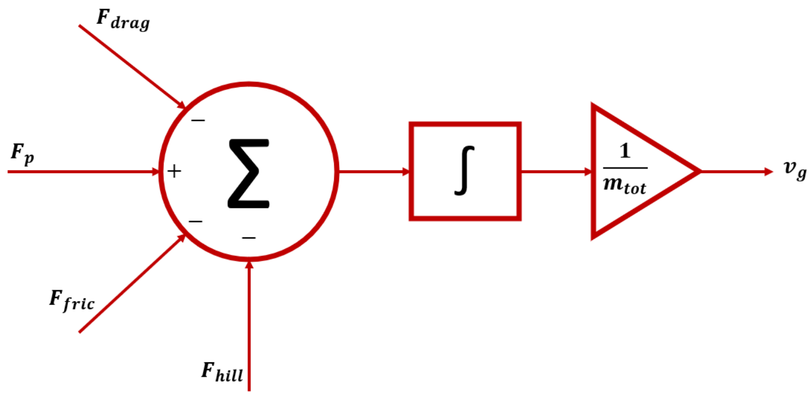

Figure 39 – Computing Velocity from Dynamic Equilibrium

Referring to the studies [40] and [39], three main driving conditions could be identified:

Table 3 – Common Driving Conditions

Case 1	Flat Ground $v_g > \sim 11\ km/h$	Air Drag Predominant $P_{drag} > P_{fric}$
Case 2	Flat Ground $v_g < \sim 11\ km/h$	Rolling Res. Pred. $P_{drag} < P_{fric}$
Case 3	Steep Hill	$P_{hill} > P_{fric} + P_{drag}$

Case 3 poses the most significant challenge for the electric powertrain. In this scenario, the power required by the motor to maintain a constant speed while driving uphill is considerably higher than that needed to overcome air resistance and friction. The same condition also arises during downhill segments, where friction and drag cannot balance out the force of gravity, and the vehicle's speed can exceed the desired range. In such situations, the electric motor must utilize the maximum available power before utilizing the mechanical brakes to slow down the vehicle and regenerate as much energy as possible through generator functioning.

Starting from these considerations, a feedback loop control system was developed outside the E.M. model.

5.2 – Vehicle Feedback Loop Model

Overall system model is designed to be modular and highly customizable; it is made by different blocks that represent different modeled parts of the system.

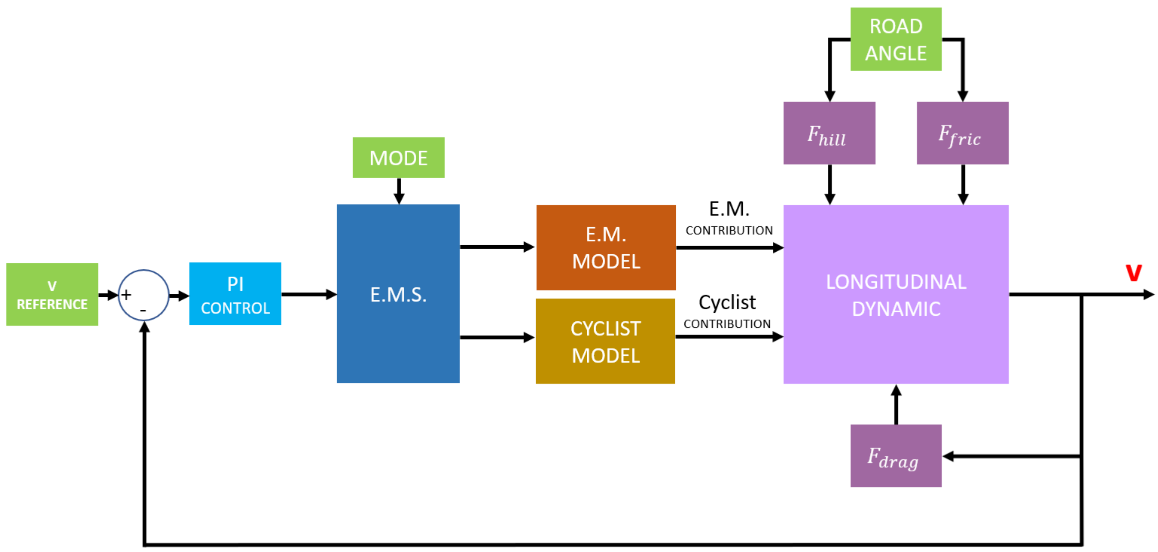

Figure 40 – Overall System Model Scheme.

The purple blocks within the system model correspond to the longitudinal dynamics of the vehicle. These dynamics are utilized to determine the speed of the system, as detailed in the preceding section.

Notably, the current iteration of the model lacks a block that characterizes the mechanical braking system. However, this can be a topic of future research endeavors, as such an inclusion could enhance the accuracy of the simulations. Currently, the cyclist block represents the mechanical braking in the model. Moreover, it is worth highlighting that the system is restricted to positive speeds and the electrical system should not function while the vehicle moves backwards.

A comprehensive exposition of each block in the system model follows.

5.2.1 – Input Block

The green blocks correspond to the system inputs. Specifically, the reference speed and the road angle inputs are obtained from experimental data. The 'mode' block is an input for the Energy Management System block and regulate the operating mode of the electric powertrain.

5.2.2 – PI Block

In light blue, the proportional-integral control block operates by receiving in input the error between the reference speed and the actual speed of the vehicle, generating a force reference. The electric powertrain and cyclist must operate synergically to generate a torque that is translated in a propulsive (or braking) force that should meet the reference force.

The gains of this block have been tuned empirically to provide the most accurate behavior [41]. The output of the block is saturated using a clamping method to avoid unrealistic force requests. The upper limit depends on the sum of the maximum torque that the motor and cyclist can produce, which are a function of the speed multiplied by appropriate conversion coefficients to transform it into forces that act on the driving wheel.

The maximum and the minimum motor torque is computed through the Torque-Angular Speed 1-D LUT seen in 4.3.2 – Control System Model. The maximum cyclist torque is computed using the model later explained in section 5.2.4 – Cyclist Model.

5.2.3 – Energy Management System (E.M.S.)

The E.M.S. block is responsible for managing the power split between the cyclist and the electric powertrain. This block takes four variables as inputs, namely the force reference output of the PI block, battery SoC, and the maximum torque that the motor can express, which is a function of the system state. The output of the E.M.S. block provides the percentage of power split between the two propulsion systems.

The control logic that handles the input variables and generates the output variables is constructed using a Stateflow block within the Simulink model. The control strategy is executed every 0.05 milliseconds to ensure quick reaction in case of sudden acceleration.

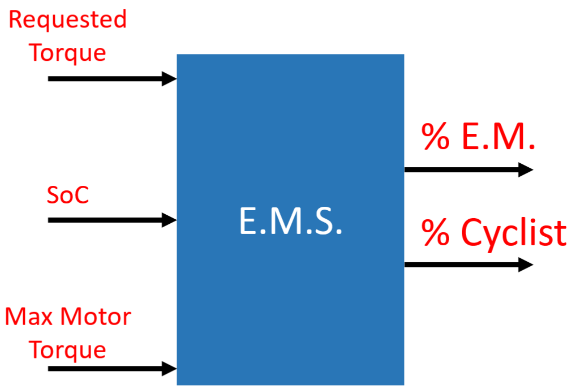

Figure 41 – Energy Management System IN and OUT variables

The E.M.S. block operates with four possible system states: IDLE, CYCLING, REGENERATIVE BRAKING and MECHANICAL ONLY BRAKING.

In the IDLE state, the control logic is inactive, and no torque is requested to the electric powertrain.

In the CYCLING state, the combined propulsion of the cyclist and the electric motor occurs, and the power split is determined based on the chosen assistance mode. Four assistance modes have been selected based on the choices of major e-bike manufacturers.

- ECO: 30% E.M., 70% Cyclist
- TRAIL: 50% E.M., 50% Cyclist
- TURBO: 66% E.M., 34% Cyclist
- OFF: Electric Powertrain is turned off, 100% Cyclist

In this state, the sum of the percentages of cyclist and electric motor must always be 100.

During REGENERATIVE BRAKING, the motor is used as a generator to produce braking torque. In this state, absolute priority is given to electric braking to recover as much energy as possible. If the braking torque of the motor is not sufficient, mechanical braking is gradually activated by simulating the cyclist squeezing the brake lever. When the braking torque of the motor becomes sufficient for braking, mechanical braking is gradually deactivated.

The state of MECHANICAL BRAKING ONLY is used to simulate the situation where the battery is sufficiently charged, and regenerative braking is bypassed. The threshold for the transition to this state is set at 95% SoC.

A functional diagram of the control logic in ECO mode is represented in Figure 42 where the four states and the transition criteria from one state to another can be distinguished.

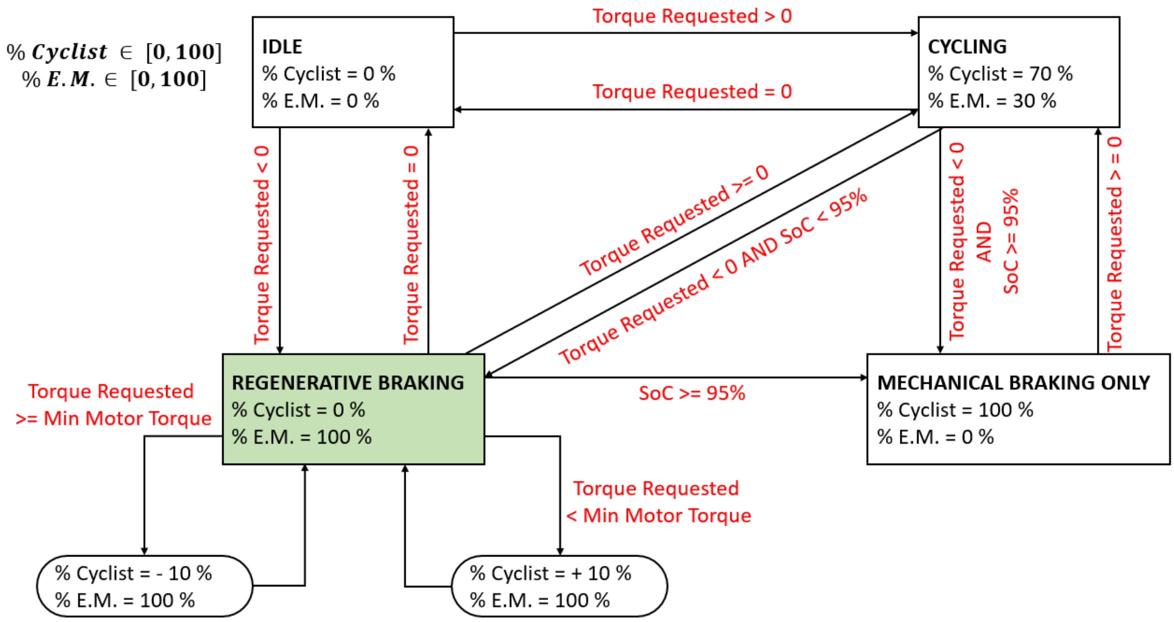

Figure 42 – E.M.S. Logic Scheme for ECO Mode.

5.2.4 – Cyclist Model

The cyclist model is only a first approximation of what could be a complete model. This block provides indications of the maximum torque that the cyclist can exert in relation to speed in order to saturate the torque with which the cyclist contributes to propulsion. The cyclist block also functions as a block for mechanical braking, but since the braking system has not been modeled, there are no lower saturation limits for "mechanical braking".

To create this model, reference was made to the study by McCartney et al. [42], in which a group of non-athletic individuals undergo an experiment to determine the relationship between cadence and maximum torque that can be exerted for short efforts (<10s).

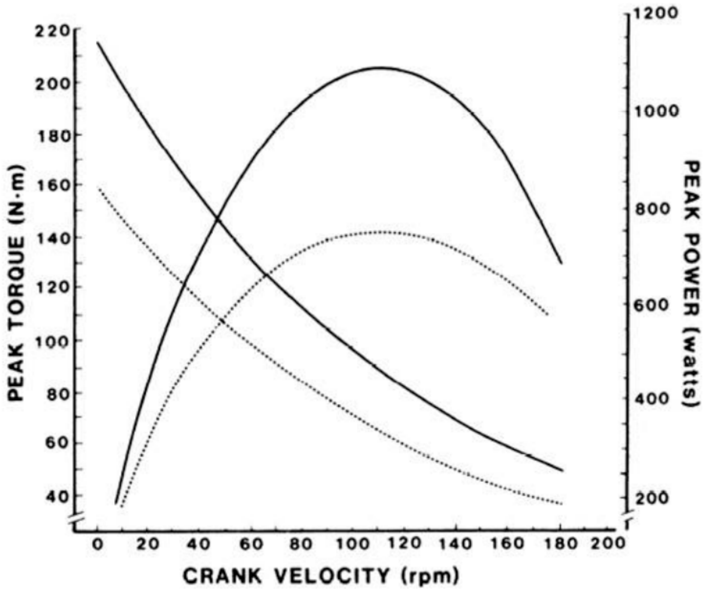

Figure 43 - Relationship between Peak Crank Torque, Cadence, and Power Output during short duration in two subjects representing the extremes of range.

Using this graph, a third-degree polynomial was constructed to approximate the cadence-torque curve. The least performant curve was chosen for more conservative simulations.

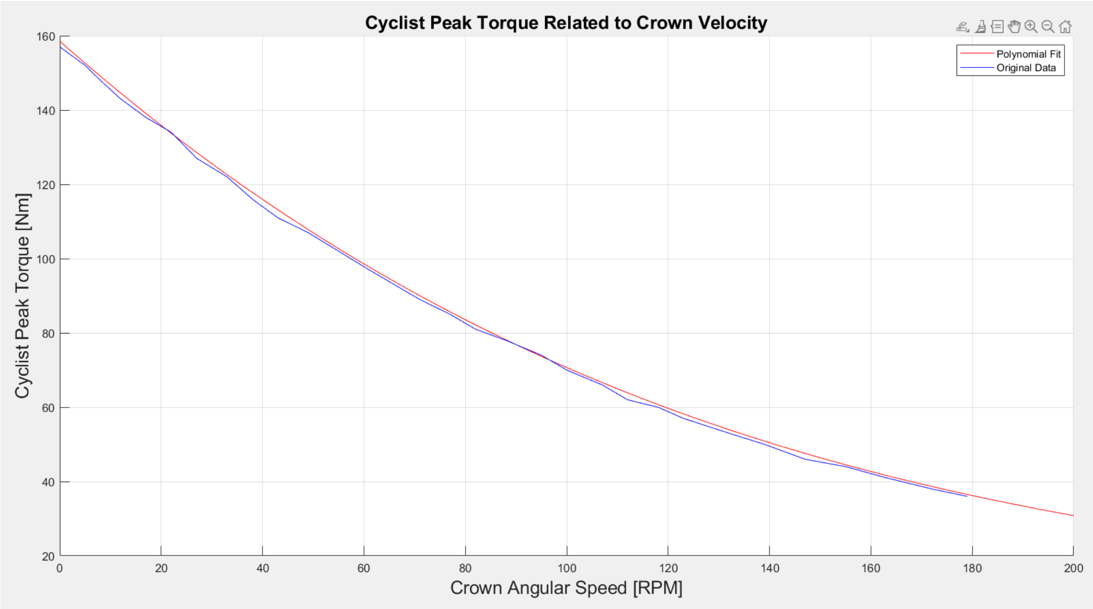

Figure 44 – 3rd Grade Polynomial Fitting Curve vs Actual Data.

CHAPTER 6 – Results

The model discussed in the previous chapters is the primary focus of this work. Its modular design enables simulation of various e-bike types on any road profile. The electric powertrain model is designed to handle a specific type of PMSM motor. Therefore, any alterations made to the electric machine configuration necessitate recalibration of the control system.

This chapter employs the model to execute simulations aimed at assessing the electric powertrain's performance. Special attention is given to evaluating the capabilities and limitations of regenerative braking. The settings of the simulations are outlined below.

6.1 – Simulations Settings

6.1.1 – Mechanical Parameters

Referring to the mechanical system configuration described in chapter 3, the overall weight of the system is fixed at 105 kg, considering 20 kg for the e-bike and 85 kg for the cyclist. All the necessary variables to define the longitudinal dynamics are evaluated referring to chapter 5 and specifically to the studies of Morchin and Oman [39]. During all the simulations, the transmission ratio between the chainring and the cassette is fixed at the 6th gear.

$$\tau_3 = \frac{\omega_{wheel}}{\omega_{pedals}} = 0.5$$

6.18

The transmission ratio between drive wheel and electric motor is fixed and equal to:

$$\tau_2 = \frac{\omega_{motor}}{\omega_{wheel}} = 30$$

6.19

Overall transmission efficiency is considered 90%.

Table 4 – Mechanical Settings.

Total Mass	kg	105
Drag Coefficient	-	1
Air Density	$\frac{kg}{m^3}$	1.2
Front Area	m^2	0.504
Rolling Friction Coefficient	-	0.0064
Transmissions Ratio (τ_3)	-	0.5
Transmissions Ratio (τ_2)	-	30
Motor Viscous Damping	$\frac{N*s}{m}$	4.924e-4

6.1.2 – Electrical Parameters

The electrical configuration refers to the system described in chapter 3. The battery starts each run with a state of charge of 77% and is kept at a temperature of 20°C throughout the simulation. To account for electrical losses in the transmission of energy, an efficiency of 85% is considered as highlighted in section 4.4 – Electric System Efficiencies.

Table 5 – Electrical Settings.

Motor	-	Ns9Nm10
Battery Capacity	Ah	18
Battery Nominal Voltage	V	36
Start SoC	%	77
Electrical Efficiency	%	85

6.1.3 – Solver Parameters

In order to carry out the simulations, the ode3 fixed-step size solver was utilized with a fundamental sample time of $T_s = \frac{1}{20000} s$. This selection was based on the Nyquist frequency, which is regarded as the switching frequency commonly used in Space Vector Pulse Width Modulation (SVPWM) techniques and is equal to 10 kHz. The fixed-step size solver provides accurate numerical approximations to the solution of the differential equations that govern the dynamics of the system.

Moreover, the choice of T_s was made in order to balance the trade-off between simulation accuracy and computational efficiency. The smaller the value of T_s, the higher the accuracy of the simulation, but this also increases the computational burden. On the other hand, a larger value leads to lower computational cost, but at the expense of simulation accuracy.

The resulting simulations provide a valuable tool for evaluating the performance of the electric powertrain under different operating conditions and can aid in the development of control strategies for e-bike applications.

6.2 – Input Data

As outlined in the preceding chapter, the model's inputs are a reference speed and the road slope. This data dynamically defines the balance of forces required to maintain accurate tracking of the reference speed.

To realistically evaluate the powertrain's behavior, it was deemed necessary to accurately select the input data to use. After testing the model with synthetized data to assure the correct functioning of the system, data from experimental acquisition are employed.

These data are collected using an e-bike with a configuration comparable to the one selected in the model and riding through different routes in such a way to cover all the possible scenarios the cyclist can encounter.

Even if this e-bike has a different electric powertrain characteristic than the one being studied, provides driving profiles compatible with the configuration under study. This approach allows for the evaluation of the powertrain's performance under real-world conditions and, on the other hand, can provide insight into the effectiveness of the model's algorithms.

Figure 45 – "STEP 1" Prototype Used for Data Acquisition.

The rider utilized a smartwatch [43] with a sampling frequency of 1 Hz to record speed, distance, and altitude signals during these routes. No wind speed is measured, so in all the simulations the wind speed is set to 0 and, consequentially, the relative velocity between the vehicle and the air is equal to the vehicle velocity.

The recorded speed serves as direct input to the model, while the altitude and distance traveled are used to determine the road slope in degrees and percentage:

$$atan2\left(\frac{\Delta Altitude}{\Delta Distance}\right) * \frac{360}{2 * \pi} = Angle\ [°]$$

$$\left(\frac{\Delta Altitude}{\Delta Distance}\right) * 100 = Slope\ [\%]$$

6.20

Since the data of Distance and Altitude suffers from noise, the computed values of road inclination profiles suffer from strong noise and numerical errors, resulting in unrealistic values not usable in the model. To tackle this problem, a custom algorithm for computing realistic values of the angle have been developed.

The signals of $\Delta Altitude$ and $\Delta Distance$ are firstly processed to eliminate outliers values, then a low-pass filter was iteratively designed and applied to both signals to eliminate noise and reduce errors. Hence, the computation of road slope is performed as shown in 6.20 and the filtered signal was then used as input for the model. The characteristics of the low pass filter used for the filtering is shown below:

$$T(s) = \frac{1}{\frac{200}{2 * \pi}s + 1}$$

6.21

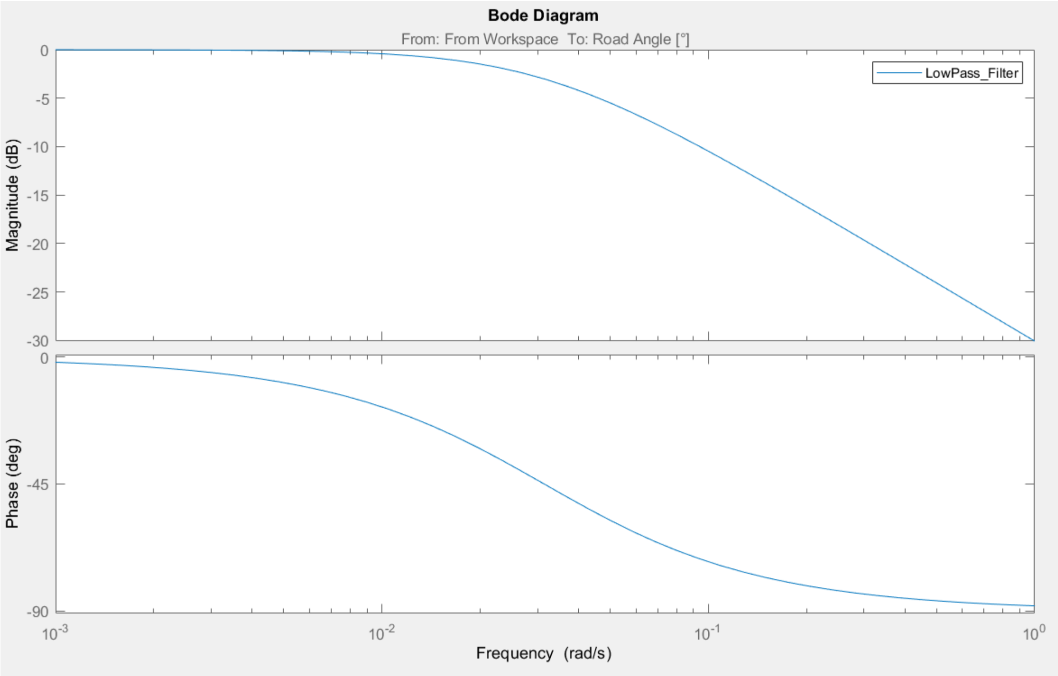

Figure 46 – Frequency Response of Low-Pass Filter 6.21.

It is worth noting that filtering introduces a phase lag to the filtered signal. Through simulations of various routes, it has been proven that the phase shift of the two signals does not significantly affect the result of simulations.

6.3 – Methods

For every profile available, four simulations were conducted. These simulations included each assistance mode that was configured in the E.M.S. block, as well as an additional simulation with the electric powertrain turned off to emulate a regular bike:

- Eco: 30% E.M.
- Trail: 50% E.M.
- Turbo: 66% E.M.
- e-Powertrain Off (r-bike): 0% E.M.

During each simulation, various data related to the dynamics of the system, such as speed, torque, and power, were recorded. Additionally, the amount of energy recovered through regenerative braking was evaluated.

6.4 – Simulations

6.4.1 – Acceleration and Braking Profile "S11U3"

The initial driving profile was obtained during a flat road test, where the operator executed acceleration and deceleration maneuvers. The vehicle reached an average top speed of 25 km/h within 13 seconds for each of the 13 cycles. In accordance with the predetermined parameters, the electric brake system was employed for all deceleration, thus resulting in energy recuperation during each cycle. The primary objective of this initial experiment was to assess the regenerative potential of the vehicle during frequent stops and starts, commonly observed in urban environments. Figure 47 depicts the progression of the 13 cycles, which occurred over a total distance of 1.15 km, completed within approximately 5 minutes.

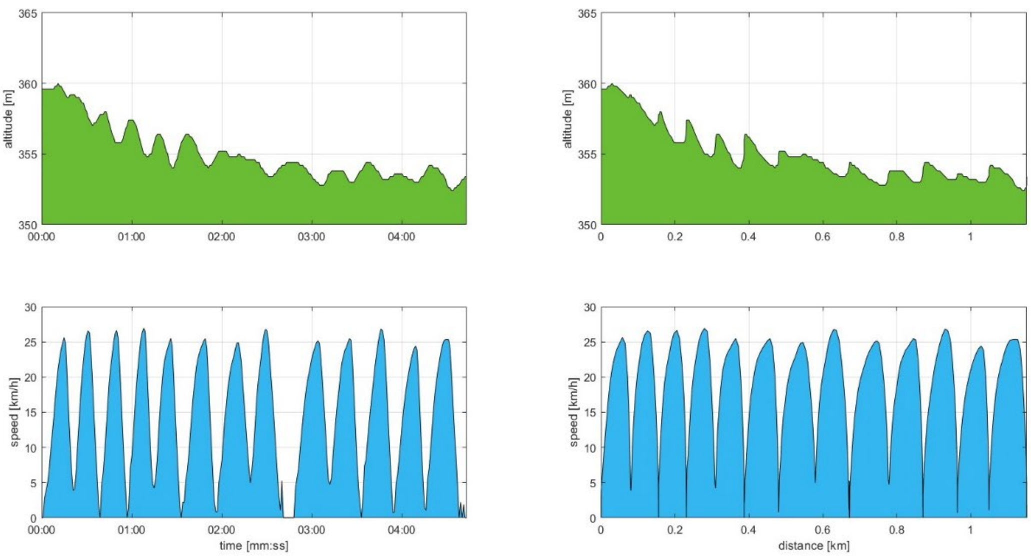

Figure 47 – Acceleration and Braking Profile "S11U3".

Table 6 - Road Profile S11U3 Data.

Average Speed	Max Speed	Average Slope	Distance	Run Time
km/h	km/h	%	km	min
15	27	+/-0	~1.15	~5

Despite the minor variations in altitude observed in the collected data, the simulations were conducted under the constraint of a road slope angle of 0%. This selection is rationalized by the purpose of the simulation, which is aimed at examining the vehicle's capacity to regenerate energy during sudden acceleration and deceleration cycles. As such, the impact of road inclination on the energy balance was deliberately eliminated.

The first simulation was conducted with the powertrain turned off to simulate a regular bicycle. In these conditions, the rider must exert a total of 55 kJ of work to perform all the cycles, while the mechanical brakes perform a total of 32 kJ of work.

Table 7 – Raw Regenerable Energy for S11U3.

MODE	E.M. Support	Cyclist Energy [kJ]	Brakes Energy [kJ]	Raw Reku Energy per Cycle
r-bike	0%	54.5	31.6	58%

This initial outcome provides an indication of the amount of work that the system must undertake and the amount of energy that can be recovered. In average, for each cycle, the system has to exert 4200 J and could recover of 2400 J.

The second simulation was conducted using the energetically most demanding Turbo profile, and the results are depicted in Figure 48. In the top left and right the instantaneous power and the work done by respectively cyclist and the motor are plotted against time. The cyclist and the motor work in synergy and express positive power in the acceleration part of each cycle and, in the deceleration segment, only the motor is active and expresses negative power due to its braking action.

In the bottom left the slope of the road is plotted against time and in the same sub-plot it is shown the variation of the Soc that has a negative trend: the battery starts at 77% and drops down to roughly 76% at the end of the route. In the bottom right the energy balance is plotted where the "Traction" bar represents the energy spent by the system to overcome the resistances and the "Reku" bar represent the regenerated energy.

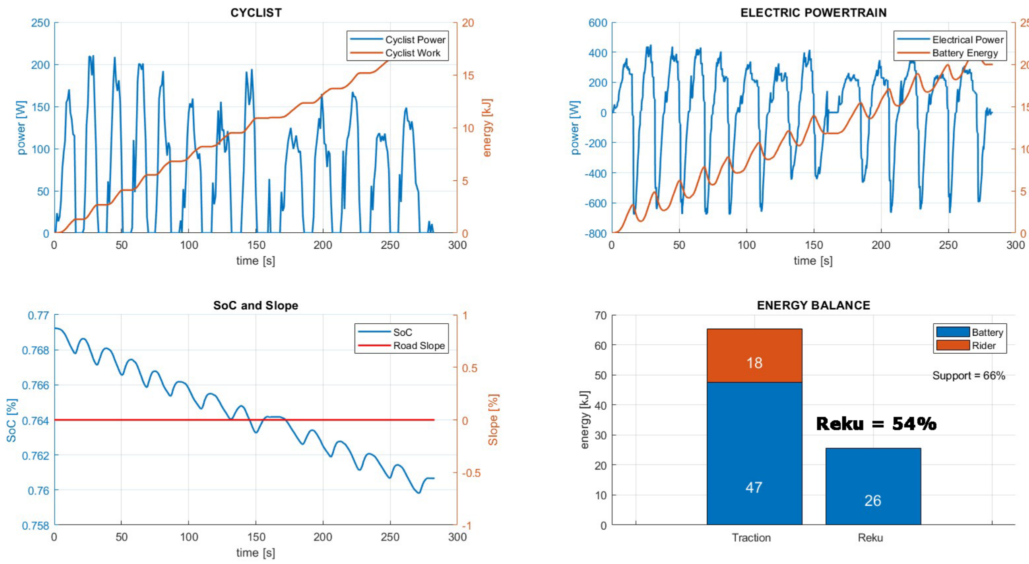

Figure 48 – Simulations Results with Turbo Mode for Profile S11U3; Reku Energy % is Referred to Battery Energy for Traction.

Table 8 - Data from S11U3 Profile in Turbo Mode Simulation.

Total Work for Traction	65 kJ		Average Motor Speed	3500 RPM
Cyclist Work	18 kJ		RMS Motor Torque	0.8 Nm
Battery Energy for Traction	47 kJ		RMS Motor Power	287 W
Mechanical Braking Work	471 J		Energy Regenerated	26 kJ

The tracking of the reference speed is faultless for the whole duration of the simulation so, also looking at the negligible work performed by the mechanical brakes, it is evident that the electric powertrain can easily handle the traction and the braking of this route.

Compared to the work executed by the brakes in the first simulation (31 kJ), the electric powertrain is capable of restoring 26 kJ. Hence, the system is capable of regenerating 54% compared to the electrical energy used for traction in each cycle or, compared to the total amount of energy spent for traction, the system can return the 39% of energy.

Table 9 – Regenerated Energy Per Cycle.

MODE	E.M. Support	Tot. Traction Energy [kJ]	Tot. Reku Energy [kJ]	Reku Energy Per Cycle vs Battery Energy	Reku Energy Per Cycle vs Total
TURBO	66%	65	25.6	54%	39%

The other assistance modes were simulated using the same profile, and the results are displayed in Table 10. Variables such as speed and acceleration remain constant, as the reference to be followed is identical, and the system is capable of achieving precise tracking.

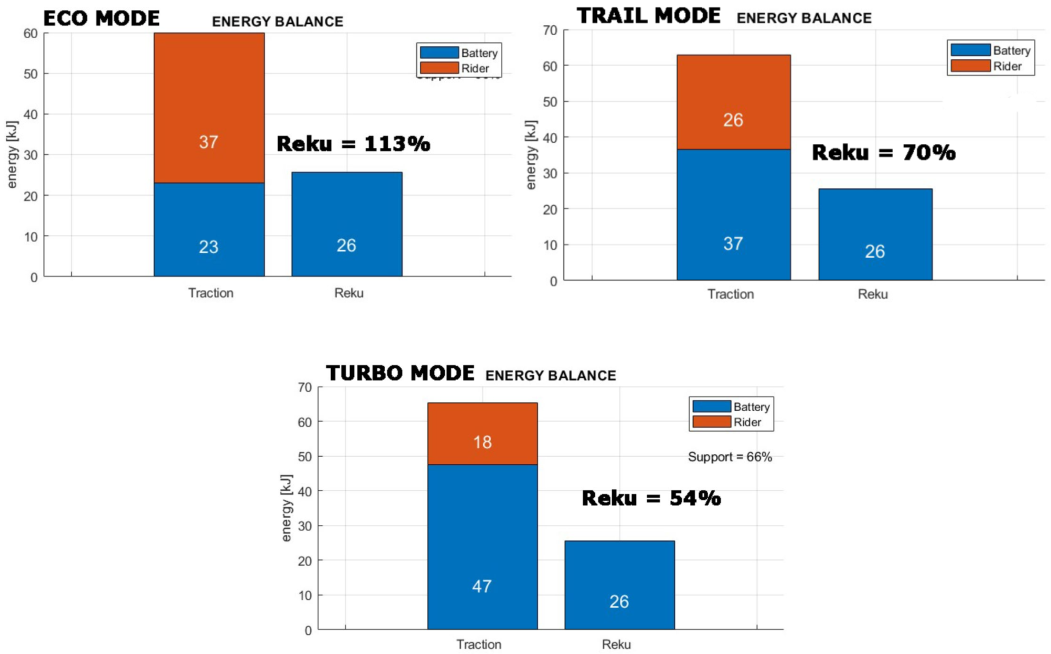

Figure 49 – Energy Balances for Eco, Trail and Turbo Modes in S11U3 Profile.

Table 10 - Eco, Trail and Turbo Mode in S11U3 Road Profile.

MODE	E.M. Support	Tot. Traction Energy [kJ]	Tot. Reku Energy [kJ]	Reku Energy vs Battery Energy Per Cycle	Reku Energy vs Total Per Cycle
ECO	30%	59.9	25.6	113%	43%
TRAIL	50%	62.8	25.6	70%	41%
TURBO	66%	65.3	25.6	54%	39%

Upon analyzing the simulation data, it is evident that the total energy consumption for traction increases slightly as the proportion of electric powertrain assistance increases. This outcome arises from the fact that the cyclist system is overall more efficient in transferring energy with respect to the electric system that has to convert energy from the battery. Nevertheless, the total amount of recuperated energy remains constant, resulting in the ratio of recovered energy to total energy remaining roughly consistent across all three modes: the system must exert an average of 4800 J and can recover 1970 J per each start and stop cycle. However, the amount of energy regenerated in proportion to the battery expenditure varies considerably across the three modes, with the Eco mode producing a positive balance and resulting in a net gain in electrical energy.

Subsequent simulations were conducted utilizing a range of road profiles that mimic realistic conditions for cycling.

6.4.2 – Mountain Profile "S1T3"

This profile is based on the data acquisition from a mountain trail consisting of both uphill and downhill segment. Throughout the route, the force generated by gravity is dominant in comparison to the forces exerted by wind and friction. Such routes are particularly demanding for both the electric powertrain and the cyclist, as they involve significant elevation changes. Furthermore, the electric system is subjected to intense stress during the downhill sections, as it is required to brake the vehicle while also maximizing energy regeneration. This type of route potentially represents an optimal condition for the implementation of regenerative braking since there is relevant potential energy to harvest and constitute the opposite situation of the previous profile since usually there frequently start and stops are absent in this kind of routes.

The analyzed path spans approximately 2.7 km of road with an altitude difference of about 100 meters. The path consists in the uphill segment traversed at a certain speed, a stall segment at about 6 minutes in which the top of the hill is reached, and finally the same road as the first segment traversed downhill at higher speed. In Figure 50 the road profile plots.

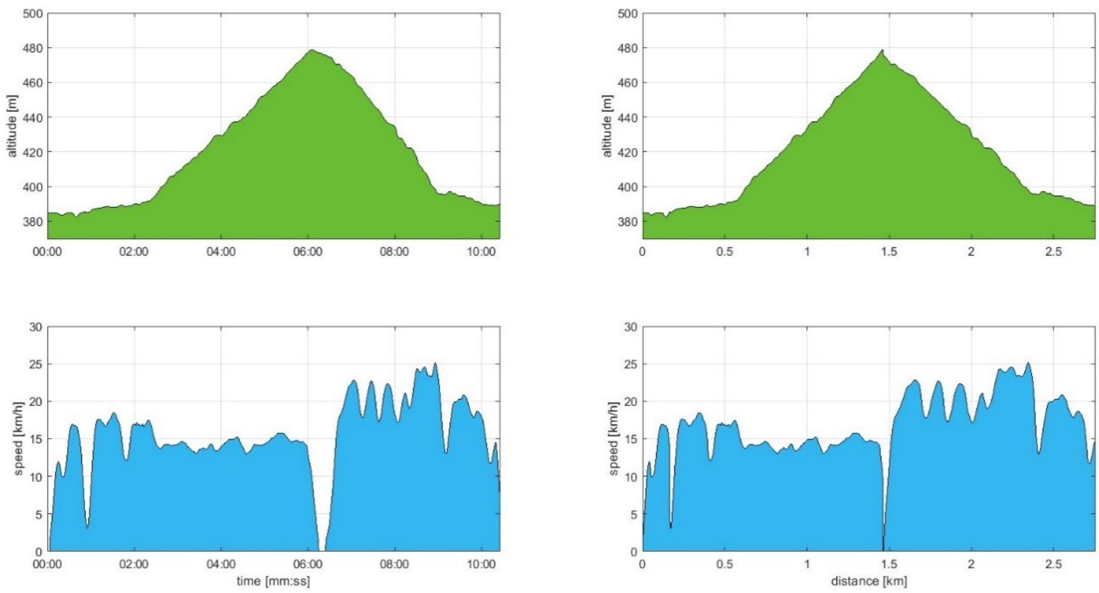

Figure 50 – Mountain Road Profile "S1_T3".

Other relevant data of this profile are shown in the following table.

Table 11 – Road Profile S1_T3 Data.

Average Climbing Speed	Average Downhill Speed	Average Climbing Slope	Average Downhill Slope	Distance	Run Time
km/h	km/h	%	%	km	min
14	17	10	-10	2.7	10

As before, the first simulation was conducted with the powertrain turned off to simulate a r-bike. In these conditions, the rider must exert 114 kJ of work to overcome the first uphill segment, while the mechanical brakes perform 73 kJ of work during the downhill section. The second simulation was conducted using the Turbo profile, and the results are depicted in Figure 51. Referring to the top left and right sub-plots, the cyclist expresses only positive power and only in the first uphill segment; the motor expresses positive electric power in the first segment where it works in synergy with the cyclist. In the downhill segment the motor expresses considerably higher negative power in absolute value since it is the main actor that brakes the vehicle.

In the bottom left the slope of the road is plotted against time to better understand the elevation profile of the trail. In the same sub-plot, it is shown the variation of the Soc: the battery starts at 77% and drops down to 73% in the traction segment; as soon as the slope became negative the battery starts recharging with the regenerative braking.

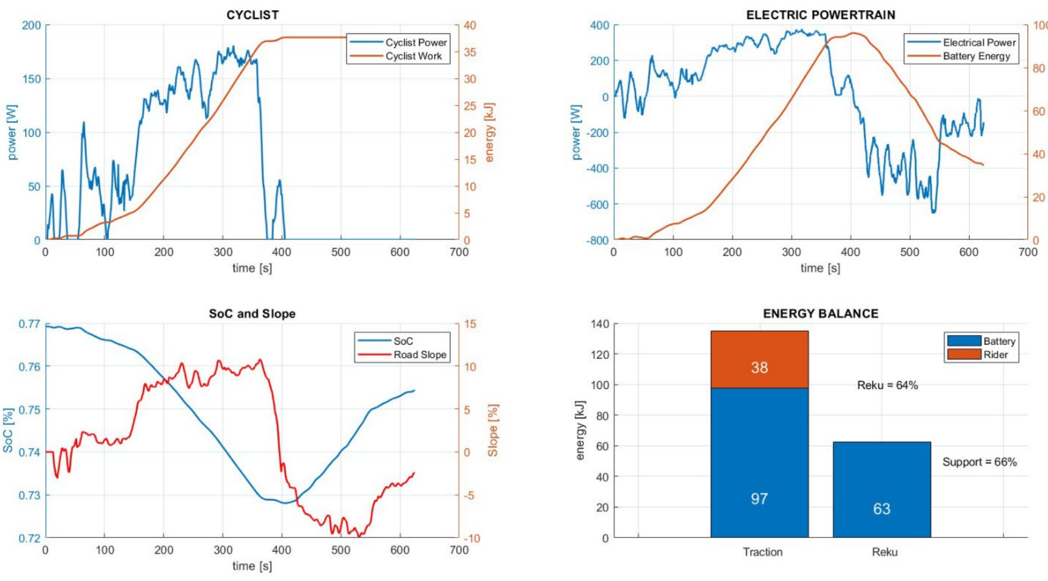

Figure 51 – Simulations Results with Turbo Mode for Profile S1_T3.

Table 12 – Data from S1_T3 Profile in Turbo Mode Simulation.

Total Work for Traction	135 kJ	Average Motor Speed	3733 RPM
Cyclist Work	38 kJ	RMS Motor Torque	0.67 Nm
Battery Energy for Traction	97 kJ	RMS Motor Power	278 W
Mechanical Braking Work	0 J	RMS Motor Climbing Power	241 W
Energy Regenerated	63 kJ	AVG Motor Downhill Power	330 W

Even in this very demanding route, the electric powertrain alone can handle the necessary power during all traction and especially braking operations, thereby regenerating a significant portion of the potential energy from the downhill segments. Compared to the work executed by the brakes in the first simulation (73 kJ), the electric powertrain is capable of regenerating 63 kJ, which corresponds to approximately 86%. Clearly, that the total energy regenerated is less than the total energy required for traction, owing to factors such as frictions and efficiencies.

Even though Turbo mode is the most energy-intensive, the regenerated electrical energy is nearly 64% of the energy requested to the battery for traction. At the end of the cycle, the battery SoC is only -1.5% respect to the start SoC.

As anticipated, the motor experiences the most significant stress during the downhill section, with an average electrical power of 330 W, as it is solely responsible for generating braking torque. In the uphill sections, the average power drops to 241 W since the motor is helped by the cyclist.

The other assistance modes were simulated using the same route, and the results are displayed in Table 13. For this longer route, it was considered more significative to report the variation in the SoC.

Table 13 – Eco, Trail and Turbo Mode in S1_T3 Road Profile.

		Regen. Braking ON		Regen. Braking OFF		
MODE	E.M. Support	ΔSoC [%]	N° Cycles	ΔSoC [%]	N° Cycles	Range Extension
ECO	30%	+0.71	INF	-2.0	50	INF
TRAIL	50%	-0.50	200	-3.2	31.3	634%
TURBO	66%	-1.5	66.6	-4.2	23.8	280%

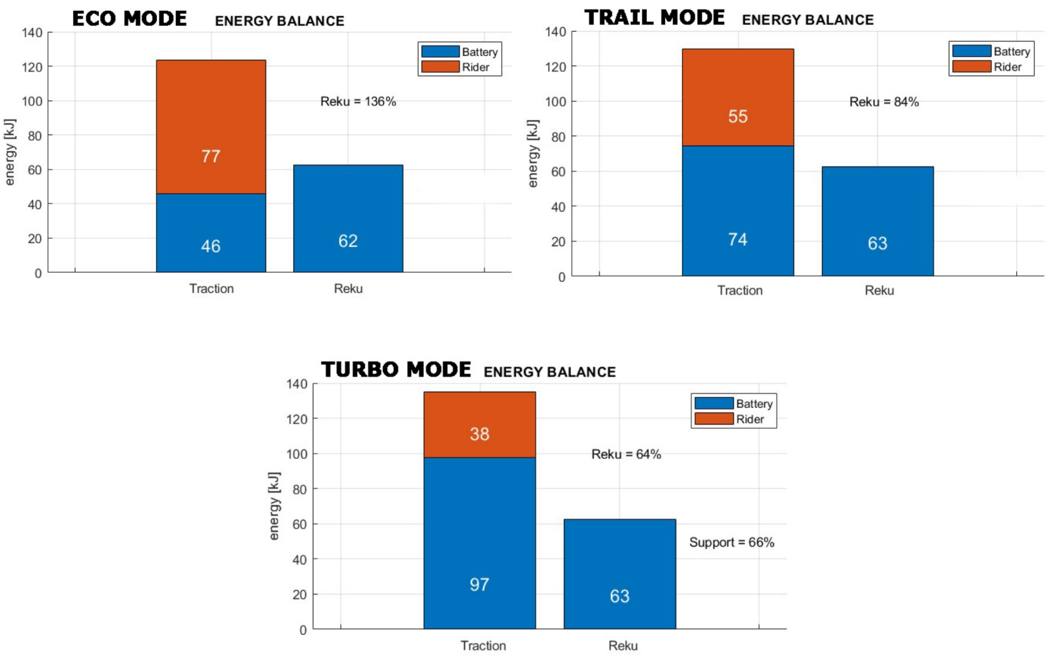

Figure 52 – Energy Balances for Eco, Trail and Turbo Modes in S1T3 Profile.

The data obtained from the simulations confirms that reducing the assistance percentage of the electric powertrain results in increased effort required from the cyclist to maintain the same speed profile, and decreases the energy requested to the battery. However, the amount of energy recovered through regenerative braking remains constant at 63 kJ, as the road profile is the same for all simulations. Hence, the ratio between the expended electrical energy and the regenerated energy changes with different assistance modes, resulting in a positive energy balance at the end of the cycle for the Eco profile, with a gain of +0.71% on the SoC. This implies that this configuration could theoretically support an infinite number of cycles without needing to be recharged and could be a significant improvement for the cyclist experience. However, it should be noted that Eco profile also require the rider to exert significantly more work compared to the other profiles.

Regarding the RMS Power of the motor, we can notice a small step of about +30 W between each mode; this is because, while the traction power significantly changes varying the assistance percentage, in the downhill segment the more relevant power of the motor is constant since the required braking torque is constant.

6.4.3 – Urban Profile "S1T10"

Urban routes pose unique challenges to electric powertrains due to the different dynamics compared to mountain routes. In an urban scenario, the route is typically longer and contains frequent starts and stops due to traffic lights or other obstacles, requiring the vehicle to overcome not only friction and wind drag but also the need for frequent acceleration and deceleration that are more relevant than the gravity force. Unlike mountain routes, there are typically no steep uphill or downhill segments that can provide large amounts of potential energy to be harvested. The demands placed on the electric powertrain are different, requiring it to provide a highly variable power output to meet the demands of the route and consequently lower regenerated energy is expected.

The road profile is depicted in Figure 53 and it is possible to notice a "serrated" speed profile, made of frequent accelerations and decelerations. On the other hand, the altitude profile varies slightly with no steep climbs or drops.

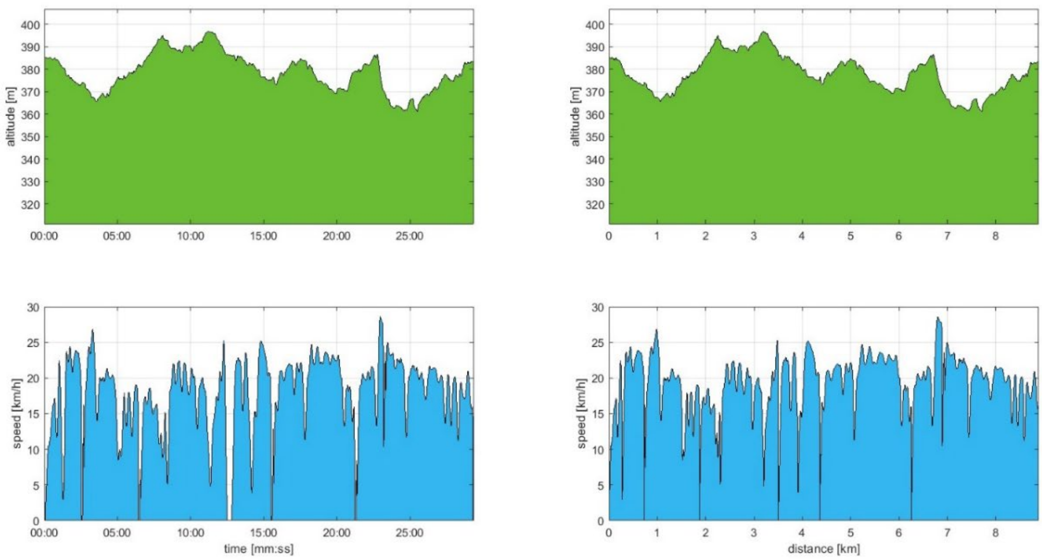

Figure 53 – Urban Road Profile "S1T10".

Table 14 – Road Profile S1_T10 Data.

Average Speed	Average Slope	Distance	Run Time
km/h	%	km	min
17	+/-2	~9	~30

In the r-bike simulation, the rider has to exert a total of 186 kJ of work to propel the bicycle, while the mechanical brakes perform 41 kJ of work. As the road profile is relatively flat, there is not much potential energy that could be harvested through regenerative braking. Therefore, only about 22% of the energy spent by the rider could theoretically be regenerated. The second simulation was carried out using the Turbo profile, which is the most energy-intensive assistance mode, as shown in Figure 54.

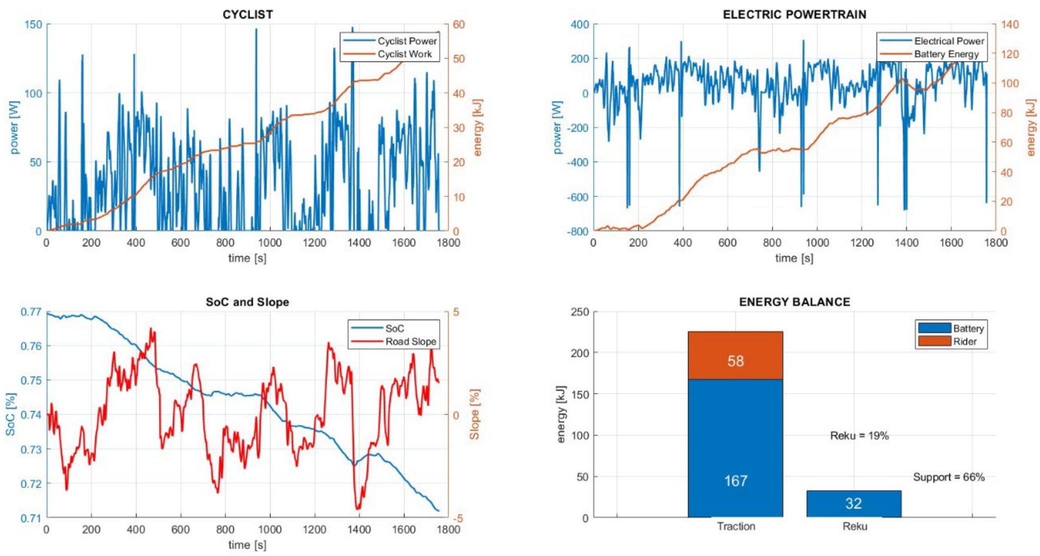

Figure 54 – Simulations Results with Turbo mode for S1T10 Road Profile.

Table 15 – Data from S1T10 Profile in Turbo Mode Simulation.

Total Work for Traction	225 kJ		Average Motor Speed	4290 RPM
Cyclist Work	58 kJ		RMS Motor Torque	0.35 Nm
Battery Energy for Traction	167 kJ		RMS Motor Power	123 W
Mechanical Braking Work	3 kJ		RMS Motor Climbing Power	-
Energy Regenerated	32 kJ		RMS Motor Downhill Power	-

It can be observed that the mechanical brakes were utilized, performing a task of 3 kJ, which is deemed negligible when compared to the work executed by the cyclist and motor. The need to use the mechanical braking is validated by the possibility of sudden obstacles, such as pedestrians or vehicles, that require prompt and forceful braking when traversing urban routes. In terms of power, this route is less demanding on the powertrain than a mountain trail as it does not entail prolonged periods of electric braking, with an average power consumption of only 137 W.

Through regenerative braking, 32 kJ of energy is produced, accounting for 78% of the previously calculated mechanical braking energy. Compared to the electrical energy expended on traction, the system recuperates 19% of the energy, concluding the driving cycle with a negative energy balance and a -5.7% SoC. The results of the other simulations are presented in Table 16.

Table 16 – Eco, Trail and Turbo Mode in S1T10 Road Profile.

		Regen. Braking ON		Regen. Braking OFF		
MODE	E.M. Support	ΔSoC [%]	N° Cycles	ΔSoC [%]	N° Cycles	Range Extension
ECO	30%	-2.4	41.7	-3.8	26.3	158%
TRAIL	50%	-4.2	23.8	-5.7	17.5	136%
TURBO	66%	-5.7	17.5	-7.1	14.1	124%

Similar to the previous scenario of S1T3 profile, reducing assistance level leads obviously to lower energy consumption from the battery. However, unlike the mountain scenario, all three modes in this case result in negative energy balance, leading lower SoC at the end of each driving cycle.

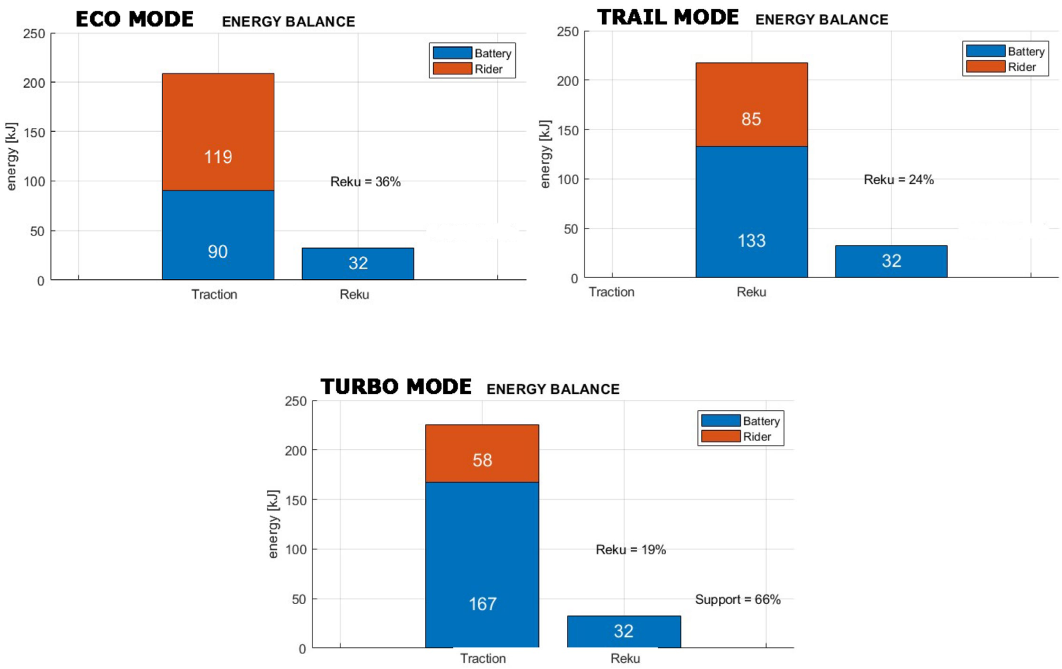

Figure 55 – Energy Balance in Eco, Trail and Turbo Modes for S1T10 Profile.

To better understand the benefit of regenerative braking in this scenario, it is useful to compare the variation in SoC with the same profiles with the regenerative braking turned Off.

In these cases, no energy is recaptured from the braking, and it is possible to observe the range of the vehicle significantly decreased. Comparing the number of cycles the vehicle can perform with starting 100% SoC, with Turbo mode up to 3 more cycles are allowed by regenerative braking, up to 6 with Trail and even 15 more cycles when using Eco mode.

6.4.4 – Long Run Profile "S11U1"

The present profile was generated using the data collected along an extended, primarily levelled path. This type of profile differs from an urban profile, given that the latter involves frequent starts and stops, whereas the former represents a cycling trip conducted outside the urban area. The absence of significant changes in elevation renders this situation unfavorable for energy recovery, as there is limited potential energy that can be transformed, and braking occurrences are scarce, unlike in city settings. Despite these unfavorable conditions, regenerative braking can still influence the vehicle's range. The illustrated path encompasses a distance of 26 km, which took 1 hour and 15 minutes to cover, with an average speed of 21 km/h.

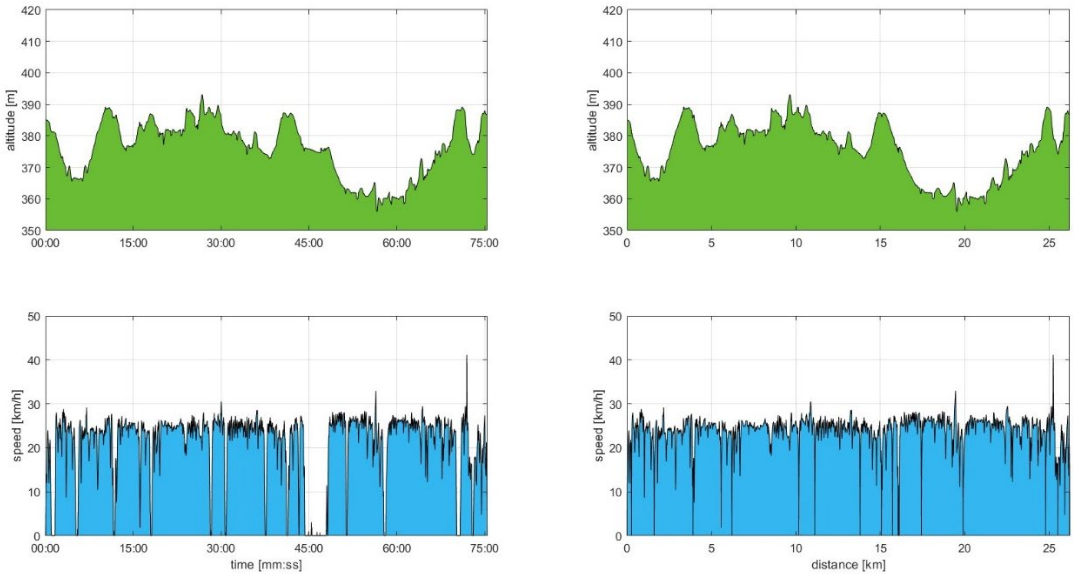

Figure 56 – Long Run Profile "S11U1".

Table 17 – Road Profile S11U1 Data.

Average Speed	Average Slope	Distance	Run Time
km/h	%	km	min
21	+/-1	~26	~75

In the r-bike simulation, the rider has to exert a total of 701 kJ of work to propel the bicycle, while the mechanical brakes perform 111 kJ of work, meaning only about 16% of the energy spent by the rider could theoretically be regenerated. The results of Turbo simulation are reported below:

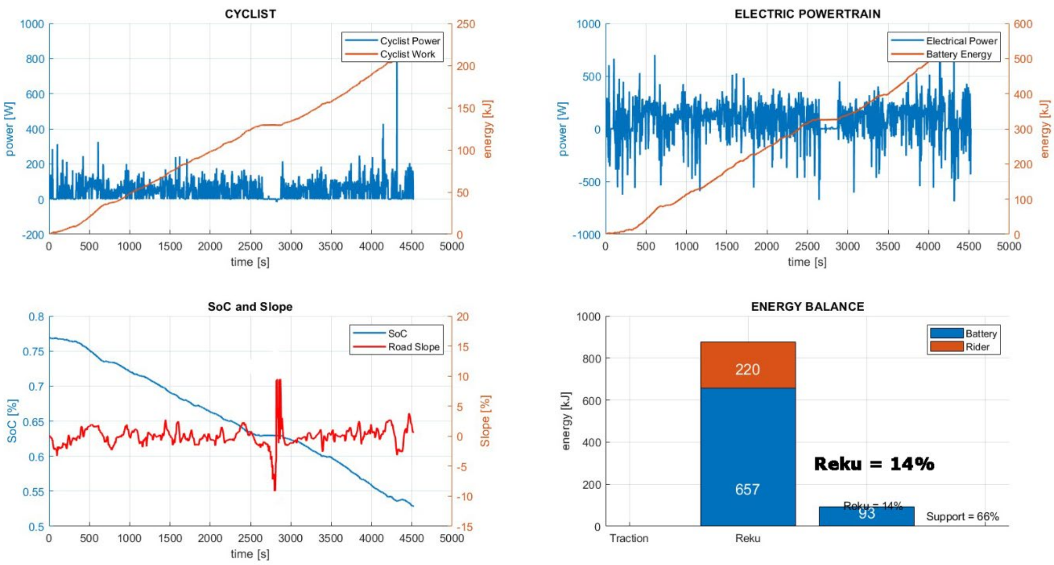

Figure 57 – Simulations Results with Turbo mode for S11U1 Road Profile.

Table 18 – Data from S11U1 Profile in Turbo Mode Simulation.

Total Work for Traction	439 kJ		Average Motor Speed	4960 RPM
Cyclist Work	220 kJ		RMS Motor Torque	0.35 Nm
Battery Energy for Traction	657 kJ		RMS Motor Power	168 W
Mechanical Braking Work	2 kJ		RMS Motor Climbing Power	-
Energy Regenerated	93 kJ		RMS Motor Downhill Power	-

Through regenerative braking, 93 kJ of energy is produced, accounting for 84% of the previously calculated mechanical braking energy.

The results of the other simulations are presented in Table 19.

Table 19 – Eco, Trail and Turbo Mode in S11U1 Road Profile.

		Regen. Braking ON		Regen. Braking OFF		
MODE	E.M. Support	ΔSoC [%]	N° Cycles	ΔSoC [%]	N° Cycles	Range Extension
ECO	30%	-11	9	-15	6.7	134%
TRAIL	50%	-18	5.6	-22	4.5	124%
TURBO	66%	-24	4.2	-28	3.6	117%

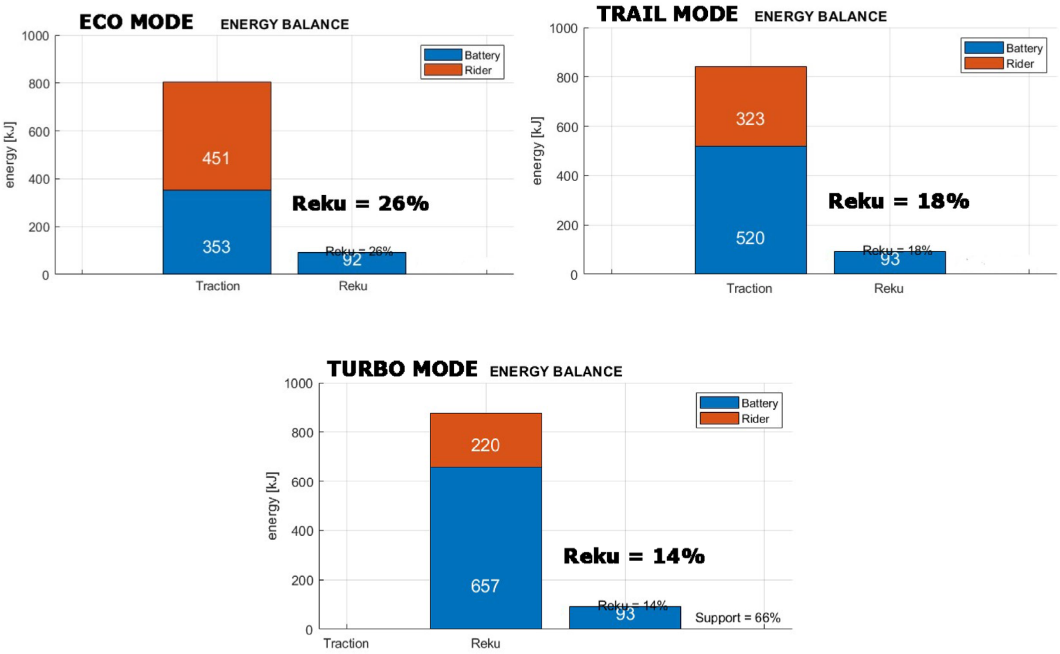

Figure 58 – Energy Balance for Eco, Trail and Turbo Modes in S11U1 Profile.

In each of the three modes, the overall energy balance is negative, indicating that none of the Modes can produce infinite number of cycles. Nevertheless, the impact of regenerative braking on energy recovery cannot be ignored. Specifically, the implementation of regenerative braking results in a notable increase in the vehicle's range, which equates to 3 more possible cycles for Eco mode and roughly 1 more cycle for both Trail and Turbo modes. These increases are not insignificant, especially considering the length of this route: even 1 more cycle means +26 km the cyclist can perform with the assistance of electric powertrain.

6.5 – Conclusions

Based on the collected data, it is evident that equipping e-bikes with regenerative braking technology could have a significant impact on extending the vehicle's range in various conditions. The advantages of regenerative braking are most pronounced during mountain routes, where the battery can be recharged during downhill sections, sometimes resulting in a greater charge level than the starting point. However, even in the other scenario where the overall energy balance is negative, the energy recovered by the motor during braking is not negligible and is translate into additional vehicle’s range. Obviously, the less power required from the motor, the more it will be able to help the cyclist for a longer period of time.

Moreover, the simulations provide insights on the performance of the electric powertrain being studied. It is shown that it can accurately meet the requirements posed by various driving routes without exerting dangerous level of power for the electrical components. Furthermore, the transmission ratio is deemed to be appropriately sized, as the motor operates predominantly within the 3000-5000 RPM range, with an average torque of less than 1 Nm, which corresponds to the motor's optimal efficiency range (Figure 59).

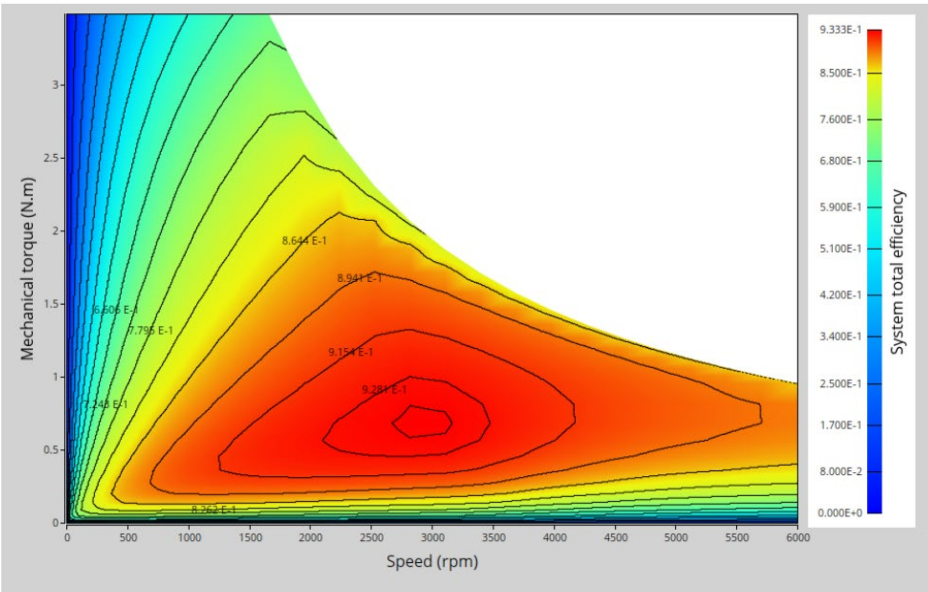

Figure 59 – Efficiency Map of the NS9SM10 Motor.

To sum up, it is possible to highlight several benefits of regenerative braking on an e-bike that could justify the additional cost and complexity of the system:

- **Increased Range**: Regenerative braking can recover energy that would otherwise be lost during braking and use it to charge the battery. The amount of energy regenerated is not negligible in any kind of scenario.

- **Reduced Brake Wear**: Electrical braking can replace the mechanical braking in the majority of cases, reducing the wear on brake pads and wheels.

- **Environmentally Friendly**: Regenerative braking reduces the amount of energy that needs to be generated and consumed, substantially increasing the number of cycles the vehicle can complete before recharging to power grid.

CHAPTER 7 – Future Developments

As explained in Chapter 2, the market for electric bicycles has experienced robust growth over the past two decades and is projected to continue to expand significantly in the future. This growth is attracting the interest of major technology and automotive companies, who are entering the market and investing in the development of new technologies aimed at enhancing the efficiency and comfort of e-bikes.

Regenerative braking technology is expected to undergo substantial development, as it offers significant advantages that outweigh the added complexity of the electric powertrain, as illustrated in the preceding chapter. However, there are numerous possibilities for improving e-bikes, including better mechanical and electrical configurations, as well as software and control logic.

Analyzing various studies, this chapter explores several potential improvements that could be further investigated in the future.

7.1 – Mid-Drive Pedelec and Regenerative Braking

One upcoming challenge is to relocate the motor from the rear wheel to the mid-drive position in electric bicycles. In doing so, the motor would be placed closer to the road and centrally located in relation to the bike, thus providing an improved weight balance and better riding experience for the rider. Furthermore, this configuration allows for the integration of the motor into the frame of the bicycle, providing better protection against dust and other external agents. As a result, the rear and front wheels of the e-bike can be easily replaced as they are identical to regular bicycle wheels.

However, incorporating regenerative braking in this type of system is significantly more complex. A possible solution is to use the same motor in a central position for both traction and regenerative braking. To achieve this, a customized gear system is necessary to allow the rider to use the bicycle normally while allowing the motor to transmit and receive power with the rear wheel. Since the same motor must generate both propulsive and braking torque on the rear wheel, the gear system must incorporate electronically controlled clutch to dynamically change the geared wheels.

7.2 – Enhanced r-bike Mode

The presented model in this thesis work allows the cyclist to switch off the electric powertrain and use the bicycle as a traditional bicycle. However, a phenomenon called Cogging Torque is always present due to the presence of the electric motor rotating with the drive wheel. The Cogging Torque produces a periodic torque that causes fatigue to the cyclist and prevents a completely smooth ride.

The Cogging Torque phenomenon occurs due to the interaction between the permanent magnets and the stator inductances. The rotation of the rotor generates a variable magnetic field that induces currents in the stator, producing a second magnetic field that interacts with the rotor's magnetic field. As a result, a periodic torque is created, as shown in Figure 60 – Cogging Torque in the NS9NM10 Motor [2].

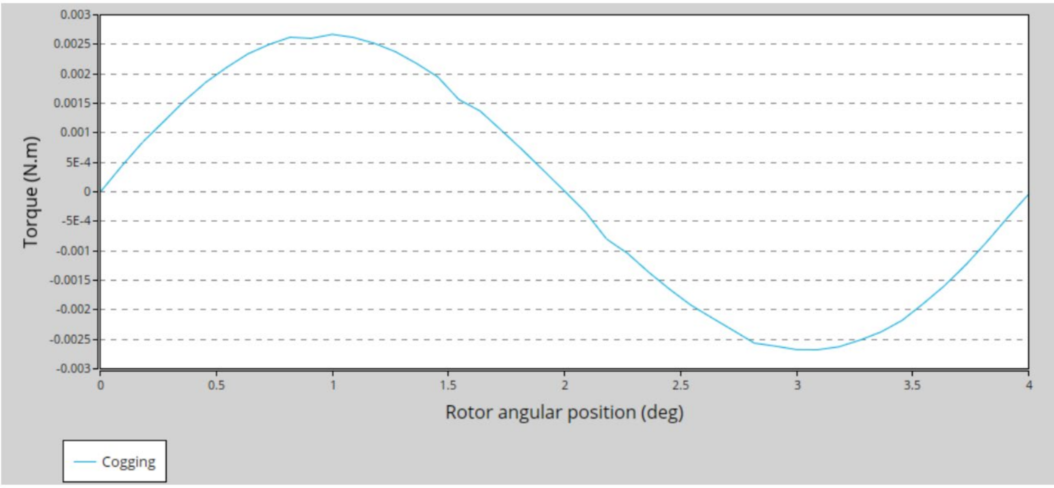

Figure 60 – Cogging Torque in the NS9NM10 Motor [2].

To address this issue, design choices can be made for the motor and its geometries, as demonstrated in the studies by Koh and Seol [44]. Additionally, complementary solutions can be implemented to further reduce the impact of Cogging Torque, such as the use of "Robust Current Injection" proposed by Liang et al. [45].

By employing these methods, it is possible to develop an additional rider-selectable riding mode, in which the control system is active and generates control input to reduce Cogging Torque without contributing to vehicle propulsion. This would enable the cyclist to use the bicycle as an e-bike in an optimal manner, while still allowing the option to switch off the electric powertrain and use it as a traditional bicycle.

7.3 – Enhanced Energy Management System

The Energy Management System described in this thesis work is based on four assistance modes, namely Eco, Trail, Turbo, and e-motor Off. The control logic considers feedback variables such as state of charge and force required to dynamically decide the power split and whether mechanical braking is necessary in addition to electric braking. However, the control logic can be further improved and refined to consider other variables such as the efficiency of the rider.

A more sophisticated control logic is drafted, which can be further developed in the future to include new riding modes that the cyclist can choose according to the usage scenario. One possible approach is to dynamically evaluate the cyclist's efficiency for each operating point and select an optimal power split.

Defining the cyclist's efficiency is not a straightforward task as it involves linking the mechanical energy output from the cyclist with the metabolic energy expended for movement. Different definitions of efficiency have been developed in various studies and are documented in the research of Lorås and Håvard Wuttudal [46].

Corno et al. [47] use heart rate measurement to estimate the cyclist's fatigue state and develop control strategies based on this variable. An interesting approach is proposed by Spagnol et al. [48], who define the cyclist's metabolic efficiency in a simplified expression:

$$\eta_{met} = \frac{E_{mech}}{\Delta V_{O_2}}$$

7.22

Where:

- E_{mech} = Output Mechanical Energy.
- ΔV_{O_2} = Cyclist's Oxygen Consumption.

This definition of metabolic efficiency is based on previous studies of the metabolic mechanisms involved in the human body during physical activity. In their research, they also conduct experimental tests to identify the zones of efficiency during pedaling, specifically by analyzing constant efforts and impulsive efforts. This approach allows for a more accurate determination of the cyclist's metabolic efficiency, which can then be used to optimize the power split between the electric motor and the cyclist's own pedaling effort in the E.M.S. By incorporating such refined control logic, it is possible to provide a more personalized and efficient riding experience for the rider.

Table 20 – Metabolic Efficiencies at Different Speed and Accelerations [48].

CONSTANT SPEED TEST RESULTS

Speed [km/h]	η_{met} [kJ/l]
12	3.87
20	4.39
25	4.37

ACCELERATION (TRANSIENT) TEST RESULTS

Max acceleration during test [g]	η_{met} [kJ/l]
0.1	2.35
0.2	2.25
0.28	1.92

Thus, there is an increase in efficiency for increasing speeds and a decrease in efficiency for increasing accelerations.

The proposed approach suggests the implementation of a driving mode that would enable the control logic to utilize efficiency points for optimal energy management. The approach would involve defining three primary conditions: Boost, Cycling, and Braking. Boost mode would be activated when strong acceleration is required, and efficiency is minimal, while Cycling mode would be activated during steady-state operation, which corresponds to maximum efficiency. Lastly, Braking mode would be activated when the system must brake and regenerate the maximum energy. The energy management system would dynamically decide the power split, based on the system state, and allocate the maximum electrical energy in Boost mode, maximum electrical braking torque in Braking mode, and gradually provide slight resistant torque to the rider when maximum efficiency is achieved to regenerate energy. Simplified graphical representations is reported in Figure 61 to illustrate the proposed system's working. In the figures negative power percentage represents negative torque expressed by the electric motor.

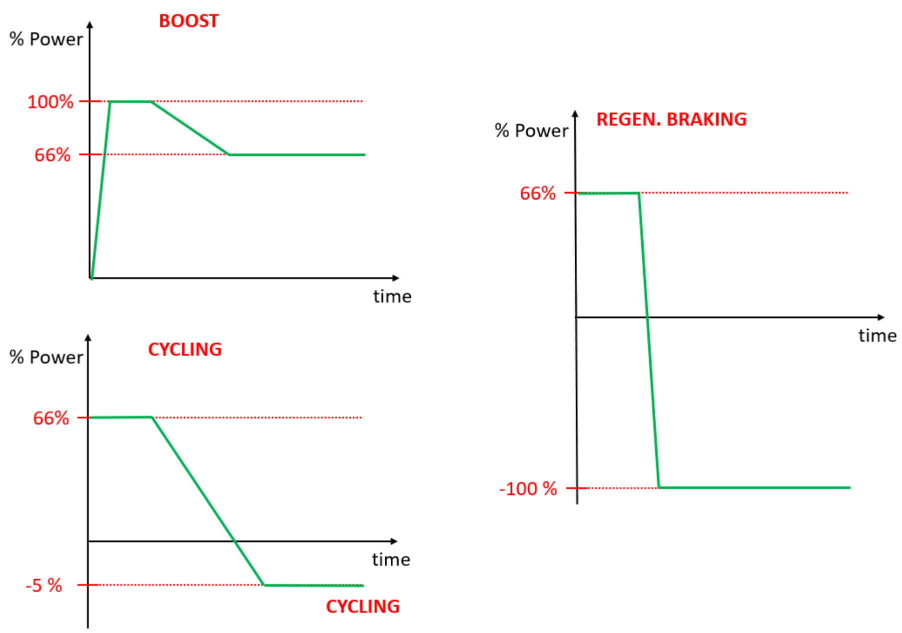

Figure 61 – Simplified Scheme of the Proposed Control Algorithm.

This could lead to a more efficient and consequently more comfortable experience for the cyclist. In fact, the proposed approach would allow for a more personalized and dynamic control of the power split, considering the rider's state and the specific operating conditions. Furthermore, this approach could potentially increase the overall efficiency of the e-bike, resulting in a longer range and improved performance.

Moreover, even more complex control strategies, similar to those used in hybrid cars, could also be explored in the future.

Nonetheless, the development of such systems would require extensive research and resources, which fall beyond the scope of this thesis.

BIBLIOGRAPHY

[1] «Sources and emissions of air pollutants in Europe — European Environment Agency». https://www.eea.europa.eu/publications/air-quality-in-europe-2021/sources-and-emissions-of-air (consultato 2 aprile 2023).

[2] E. C. Zenerino, «Ns9Nm10_eBike».

[3] G. Italia, «INQUINAMENTO ATMOSFERICO E CAMBIAMENTI CLIMATICI Elementi per una strategia nazionale di prevenzione».

[4] J. Pielecha, J. Merkisz, R. Jasiński, e W. Gis, «Real Driving Emissions Testing of Vehicles Powered by Compressed Natural Gas», presentato al JSAE/SAE 2015 International Powertrains, Fuels & Lubricants Meeting, set. 2015, pp. 2015-01–2022. doi: 10.4271/2015-01-2022.

[5] Legambiente, «Mal'aria di città • Legambiente», *Legambiente*, 30 gennaio 2023. https://www.legambiente.it/rapporti-e-osservatori/rapporti-in-evidenza/malaria-di-citta/ (consultato 19 febbraio 2023).

[6] «EU ban on sale of new petrol and diesel cars from 2035 explained | News | European Parliament», 3 novembre 2022. https://www.europarl.europa.eu/news/en/headlines/economy/20221019STO44572/eu-ban-on-sale-of-new-petrol-and-diesel-cars-from-2035-explained (consultato 22 febbraio 2023).

[7] J. Y. Yong, V. K. Ramachandaramurthy, K. M. Tan, e N. Mithulananthan, «A review on the state-of-the-art technologies of electric vehicle, its impacts and prospects», *Renew. Sustain. Energy Rev.*, vol. 49, pp. 365–385, set. 2015, doi: 10.1016/j.rser.2015.04.130.

[8] R. L. Abduljabbar, S. Liyanage, e H. Dia, «The role of micro-mobility in shaping sustainable cities: A systematic literature review», *Transp. Res. Part Transp. Environ.*, vol. 92, p. 102734, mar. 2021, doi: 10.1016/j.trd.2021.102734.

[9] C. R. Cherry, J. X. Weinert, e Y. Xinmiao, «Comparative environmental impacts of electric bikes in China», *Transp. Res. Part Transp. Environ.*, vol. 14, fasc. 5, pp. 281–290, lug. 2009, doi: 10.1016/j.trd.2008.11.003.

[10] M. Weiss, P. Dekker, A. Moro, H. Scholz, e M. K. Patel, «On the electrification of road transportation – A review of the environmental, economic, and social performance of electric two-wheelers», *Transp. Res. Part Transp. Environ.*, vol. 41, pp. 348–366, dic. 2015, doi: 10.1016/j.trd.2015.09.007.

[11] A. Muetze e Y. Tan, «Electric bicycles - A performance evaluation», *IEEE Ind. Appl. Mag.*, vol. 13, fasc. 4, pp. 12–21, lug. 2007, doi: 10.1109/MIA.2007.4283505.

[12] «Regolamento (UE) n. 168/2013 del Parlamento europeo e del Consiglio, del 15 gennaio 2013, relativo all'omologazione e alla vigilanza del mercato dei veicoli a motore a due o tre ruote e dei quadricicliTesto rilevante ai fini del SEE».

[13] L. Stilo, D. Segura-Velandia, H. Lugo, P. P. Conway, e A. A. West, «Electric bicycles, next generation low carbon transport systems: A survey», *Transp. Res. Interdiscip. Perspect.*, vol. 10, p. 100347, giu. 2021, doi: 10.1016/j.trip.2021.100347.

[14] C. Contò e N. Bianchi, «E-Bike Motor Drive: A Review of Configurations and Capabilities», *Energies*, vol. 16, fasc. 1, p. 160, dic. 2022, doi: 10.3390/en16010160.

[15] M. Corno, F. Roselli, e S. M. Savaresi, «Bilateral Control of SeNZA—A Series Hybrid Electric Bicycle», *IEEE Trans. Control Syst. Technol.*, vol. 25, fasc. 3, pp. 864–874, mag. 2017, doi: 10.1109/TCST.2016.2587243.

[16] O. Bolton, «Electrical Bicycle; Patent No. 552 271».

[17] «1993 PAS (PA26-A) - Communication Plaza | Yamaha Motor Co., Ltd.» https://global.yamaha-motor.com/showroom/cp/collection/pas_pas_pa26-a/ (consultato 21 febbraio 2023).

[18] A. R. Cooper *et al.*, «Potential of electric bicycles to improve the health of people with Type 2 diabetes: a feasibility study», *Diabet. Med. J. Br. Diabet. Assoc.*, vol. 35, fasc. 9, pp. 1279–1282, mag. 2018, doi: 10.1111/dme.13664.

[19] J. E. Bourne *et al.*, «Health benefits of electrically-assisted cycling: a systematic review», *Int. J. Behav. Nutr. Phys. Act.*, vol. 15, fasc. 1, p. 116, dic. 2018, doi: 10.1186/s12966-018-0751-8.

[20] B. de Geus, F. Kempenaers, P. Lataire, e R. Meeusen, «Influence of electrically assisted cycling on physiological parameters in untrained subjects», *Eur. J. Sport Sci.*, vol. 13, fasc. 3, pp. 290–294, mag. 2013, doi: 10.1080/17461391.2011.606845.

[21] «Different Types of Electric Bikes Explained», *Bikexchange*. https://bikexchange.com/types-of-electric-bikes/ (consultato 20 febbraio 2023).

[22] «E-bikes Market Size, Share|Industry Report, 2022-2030». https://www.grandviewresearch.com/industry-analysis/e-bikes-market-report (consultato 22 febbraio 2023).

[23] N. B. Hung e O. Lim, «A review of history, development, design and research of electric bicycles», *Appl. Energy*, vol. 260, p. 114323, feb. 2020, doi: 10.1016/j.apenergy.2019.114323.

[24] «Bosch eBike Systems | Premium drives for eBikes & Pedelecs», *Bosch eBike Systems*. https://www.bosch-ebike.com/en/ (consultato 22 febbraio 2023).

[25] «Mtb Rockrider ST 530 grigia 27,5"». https://www.decathlon.it/p/mtb-rockrider-st-530-grigia-27-5/_/R-p-311274 (consultato 7 febbraio 2023).

[26] F. Cupertino, «AZIONAMENTI ELETTRICI».

[27] W. L. Soong e T. J. E. Miller, «Theoretical limitations to the field-weakening performance of the five classes of brushless synchronous AC motor drive», in *1993 Sixth International Conference on Electrical Machines and Drives (Conf. Publ. No. 376)*, set. 1993, pp. 127–132.

[28] Q. Yang, Z. Kang, M. Zhang, e N. Zhao, «Study on space vector PWM technology of PMSM control system based on dSPACE», in *2013 IEEE International Conference on Information and Automation (ICIA)*, Yinchuan, China: IEEE, ago. 2013, pp. 576–580. doi: 10.1109/ICInfA.2013.6720363.

[29] «Modeling of speed distribution for mixed bicycle traffic flow». https://journals.sagepub.com/doi/epub/10.1177/1687814015616918 (consultato 6 febbraio 2023).

[30] L. Frosini, «Ripasso sul campo magnetico rotante e avvolgimenti in corrente alternata».

[31] M. Bhardwaj, «Sensored Field Oriented Control of 3-Phase Permanent Magnet Synchronous Motors», 2013.

[32] R. Krishnan, *Permanent Magnet Synchronous and Brushless DC Motor Drives*, 1ª ed. CRC Press, 2017. doi: 10.1201/9781420014235.

[33] R. Galluzzi, «Slides from Brushless PM Motor Design Workshop». 19 ottobre 2022.

[34] «Three-phase interior permanent magnet synchronous motor with sinusoidal back electromotive force - Simulink - MathWorks Italia». https://it.mathworks.com/help/autoblks/ref/interiorpmsm.html (consultato 14 febbraio 2023).

[35] «Electric Rotating Motor Design | FluxMotor», *Default*. https://altair.com/fluxmotor (consultato 22 marzo 2023).

[36] R. Galluzzi, «PMSM Model and Control». 11 2022.

[37] «Lithium-ion, lithium-polymer, or lead-acid battery - Simulink - MathWorks Italia». https://it.mathworks.com/help/autoblks/ref/datasheetbattery.html (consultato 15 febbraio 2023).

[38] J. J. Taborek, *Mechanics of Vehicles*.

[39] W. C. Morchin e H. Oman, «Electric Bycycles: A Guide to Design and Use», 2006.

[40] A. Muetze e Y. C. Tan, «Performance evaluation of electric bicycles», in *Fourtieth IAS Annual Meeting. Conference Record of the 2005 Industry Applications Conference, 2005.*, Hong Kong, China: IEEE, 2005, pp. 2865–2872. doi: 10.1109/IAS.2005.1518866.

[41] K. M. Lynch, N. Marchuk, e M. L. Elwin, *Embedded computing and mechatronics with the PIC32 microcontroller*. Amsterdam: Elsevier, 2016.

[42] N. McCartney, G. Obminski, e G. J. Heigenhauser, «Torque-velocity relationship in isokinetic cycling exercise», *J. Appl. Physiol.*, vol. 58, fasc. 5, pp. 1459–1462, mag. 1985, doi: 10.1152/jappl.1985.58.5.1459.

[43] Garmin e G. L. or its subsidiaries, «GARMIN | fēnix® 6S Pro e Sapphire | Orologio GPS multisport», *Garmin*. https://www.garmin.com/it-IT/p/641530 (consultato 19 marzo 2023).

[44] Chang Seop Koh e Jin-Soo Seol, «New cogging-torque reduction method for brushless permanent-magnet motors», *IEEE Trans. Magn.*, vol. 39, fasc. 6, pp. 3503–3506, nov. 2003, doi: 10.1109/TMAG.2003.819473.

[45] Q. Liang, F. Wei, Z. Li, Y. Deng, e Y. Wang, «Torque Ripple Suppression of Permanent Magnet Synchronous Motor Based On Robust Current Injection», *IOP Conf. Ser. Mater. Sci. Eng.*, vol. 782, fasc. 3, p. 032082, mar. 2020, doi: 10.1088/1757-899X/782/3/032082.

[46] G. Ettema e H. W. Lorås, «Efficiency in cycling: a review», *Eur. J. Appl. Physiol.*, vol. 106, fasc. 1, pp. 1–14, mag. 2009, doi: 10.1007/s00421-009-1008-7.

[47] M. Corno, P. Giani, M. Tanelli, e S. M. Savaresi, «Human-in-the-Loop Bicycle Control via Active Heart Rate Regulation», *IEEE Trans. Control Syst. Technol.*, vol. 23, fasc. 3, pp. 1029–1040, mag. 2015, doi: 10.1109/TCST.2014.2360912.

[48] P. Spagnol *et al.*, «A full hybrid electric bike: How to increase human efficiency», in *2012 American Control Conference (ACC)*, Montreal, QC: IEEE, giu. 2012, pp. 2761–2766. doi: 10.1109/ACC.2012.6314871.